The effect of melt composition and oxygen fugacity on manganese partitioning between apatite and silicate melt

Declarations of interest: none

The effect of melt composition and oxygen fugacity on manganese partitioning between apatite and silicate melt

T.N. Stokes[1]*, G. D. Bromiley[1], N. J. Potts[1], K. E. Saunders[1], A. J. Miles[2], EIMF[1]

[1]School of GeoSciences, Grant Institute, Kings Buildings, University of Edinburgh, Edinburgh, UK.

[2]School of Geography, Geology and the Environment, University of Leicester, University Road, Leicester LE1 7RH, UK

*Corresponding Author: thomas.stokes@ed.ac.uk

Abstract:

Oxygen fugacity and melt composition are both known to have a strong influence on the partitioning of trace elements between coexisting minerals and melt. Previous work has suggested that Mn partitioning between apatite and silicate melt may be strongly affected by oxygen fugacity and could, therefore, act as an oxybarometer. Here, we present a new study on the partitioning of Mn between apatite and melt at high temperature (1400-1250 °C) and 1 GPa pressure, for various melt compositions and oxygen fugacities (NNO +4.7 to NNO -10). We find that there is no demonstrable variation in the partition coefficient for Mn between apatite and silicate melt ($D_{Mn}^{Ap\text{-}m}$) across the range of fO_2 conditions studied here. Instead, we find that $D_{Mn}^{Ap\text{-}m}$ varies significantly with melt composition and that in particular, the proportion of non-bridging oxygens strongly influences partitioning of Mn between apatite and melt. We propose that variations in the Mn content of natural apatite, previously thought to reflect variations in fO_2, are instead related to the degree of melt polymerization. These findings are consistent with the results of Mn K-edge XANES spectroscopy, which demonstrate that Mn in coexisting apatite and silicate glass is present predominantly as Mn^{2+} regardless of fO_2. Furthermore, XANES spectra from a series of silicate glasses synthesised at various oxygen fugacities demonstrate that Mn^{2+} is the predominant species, and that the average Mn oxidation state does not vary over a wide range of fO_2-T conditions.

Keywords: Apatite, Manganese, element partitioning, oxygen fugacity, experimental petrology, melt composition

Introduction:

Apatite [nominally $Ca_5(PO_4)_3(F,Cl,OH)$] is an accessory mineral found in many igneous, metamorphic, and sedimentary rocks. The three primary apatite end-members (fluor-, chlor- and hydroxyapatite) relate to the three anion end members of apatite (F, Cl and OH respectively). The incorporation of these volatiles as major constituents in the apatite crystal structure make it a critical mineral for understanding melt volatile contents in terrestrial (Douce and Roden 2006; Scott et al. 2015) and extra-terrestrial systems (Gross et al. 2013; McCubbin et al. 2016). Apatite is also an important tool for exploring the trace element budgets of magmas (Nagasawa 1970; Sha and Chappell 1999), as its crystallographic structure allows for the incorporation of more than half the stable naturally-occurring elements (Hughes 2015). Recent work (Miles et al. 2014; Konecke et al. 2017) has also suggested that the substitution of redox sensitive elements (e.g. Mn, S, Ce, Eu) into apatite could be used to constrain the oxygen fugacity (fO_2) of the melt from which it has crystallized, providing a much needed new oxybarometer.

Oxygen fugacity is an important parameter within igneous systems because, among other things, it controls mineral stabilities (Hensen 1986; Toplis and Carroll 1995), dictates gas species released from volcanoes (Wallace and Carmichael 1992; Moussallam et al. 2016), and has implications on the metallogenesis of primary igneous ore bodies (Fleet et al. 1991). Furthermore, estimates of fO_2 are used in modelling geophysical processes in the mantle (e.g. creep, electrical conductivity; Ryerson et al. 1989; Wood and Nell 1991; Dai and Karato 2014) and understanding the timing of planetary scale processes, such as the oxidation of the mantle and atmosphere (Scaillet and Gaillard 2011). Oxygen fugacity is also an important variable when constraining the composition of the earth's core (Li and Agee 2001) and early continental crust (Yang et al. 2014), as well as for the timing of the onset of plate tectonics (Brounce et al. 2015). However, despite the importance of fO_2 it remains one of the most

difficult geological parameters to accurately constrain. As such, any dependence of chemical substitutions in apatite on fO_2 would be invaluable in constraining planetary processes.

Manganese in apatite is a minor element that can substitute for more than 1 atom per formula unit (a.p.f.u.) onto the Ca2 and P sites (Hughes et al. 2004; Deer et al. 2013). Several studies have indicated that while partitioning of Mn between apatite and silicate melt is sensitive to oxygen fugacity, it is also dependent on parameters such as melt SiO_2 and total alkali content, as well as melt structure (Sha and Chappell 1999; Belousova et al. 2001; Chu et al. 2009; Miles et al. 2014). This work aims to constrain the sensitivity of Mn partitioning between apatite and melt to fO_2 for a variety of silicate melt compositions and to assess its viability as an oxybarometer.

1.1 Experimental rational

We primarily set out to test the conclusion of Miles et al. (2014) that the Mn content of apatite, from a range of calc-alkaline intermediate to silicic rocks, can be directly related to fO_2 via the below empirical relationship:

$$\log fO_2 = -0.0022\ (\pm 0.0003)\ Mn\ (ppm) - 9.75\ (\pm 0.46) \quad [1]$$

This dependence implies that variations in fO_2 influence Mn apatite-melt partitioning because of a change in the relative proportions of Mn oxidation states in the melt (Mn can be found in the 2+, 3+, 4+, and 5+ oxidation states in nature). However, under most geological conditions, Mn^{2+} is by far the dominant species in silicate melts (Watson 1977, Schmidt et al. 2006). In apatite, Mn^{2+} has an ionic radius of 0.90 Å in 7-fold (Shannon 1976) and 1.0 Å in 9-fold coordination (Miles et al. 2014). The corresponding values for Ca^{2+} are 1.06 Å and 1.18 Å (Shannon 1976). Mn^{3+} has a smaller ionic radius (0.62-0.67 Å; Miles et al. 2014); hence Mn^{2+} should preferentially partition into apatite from the melt compared to Mn^{3+}. However, Marks et al (2016) questioned the general applicability of a Mn-in-apatite oxybarometer, suggesting that additional controls such as temperature, melt composition and the co-precipitation of other Mn-bearing phases may also influence the Mn content of natural apatites.

We have conducted an experimental calibration of Mn oxidation state in silicate melts as a function of fO_2, in order to investigate its impact on apatite-melt partitioning. Experiments were designed to examine how Mn oxidation state, in both apatite and melt, vary as a function of fO_2 for a range of melt compositions. Apatite in three end-member melt compositions, ranging from basaltic andesite to rhyolitic, were chosen so that any effects of crystal chemistry and melt composition on Mn partitioning could also be determined.

1.2 Starting Materials

Starting materials consisted of mixtures of high-purity analytical oxide (SiO_2, Al_2O_3, TiO_2, MgO, Fe_2O_3, MnO_2) and carbonate ($CaCO_3$, Na_2CO_3, and K_2CO_3) powders. Before use, powders were fired using the following conditions: SiO_2 8 hours 1250 °C, TiO_2 16 hours 1000 °C, Al_2O_3 18 hours 1250 °C, Fe_2O_3 1 hour 800 °C, MgO 18 hours 1250 °C, $CaCO_3$ 4 hours 400 °C, Na_2CO_3 12 hours 400 °C and K_2CO_3 8 hours 500°C. Following firing, powders were stored in a 110 ℃ oven. The starting compositions were ground under acetone, using an agate mortar and pestle, for thirty minutes, to ensure homogeneity. Powders were then loaded in a box furnace and decarbonated using a controlled heating program, which ramped the temperature from 600- to 1000 ° C over a 6 hour period. Following decarbonation, an apatite component consisting of various amounts of tri-calcium phosphate [TCP- $Ca_3(PO_4)_2$] and either CaF_2 or $CaCl_2$ was added to the starting material, and the mixture was reground for a further thirty minutes in acetone. At this stage, water (1.5 wt. % H_2O) was also added to the SH3 and BMT2 starting compositions in the form of gibbsite ($Al(OH)_3$) or brucite ($Mg(OH)_2$). The different bulk starting compositions used in this study can be found in Table 1. Note PM1 and HAP10 were two iterations of the same starting compositions.

1.3 Experimental Procedures

Experiments were carried out in an end-loaded piston cylinder, using ½" talc-pyrex assemblies with an internal graphite resistance furnace, and inner crushable alumina spacers. Runs were first pressurised to ~0.3 GPa before heating, then pressurised simultaneously with temperature, which was raised at a

rate of 100 °C/min. After reaching super liquidus conditions runs were slightly over pressurised to compensate for pressure loss during the first hour (hot piston out technique). Temperature was continuously monitored using a $Pt_{100-}Pt_{87}Rh_{13}$ thermocouple placed ≈10 °C from the hot spot of the assembly. All experiments were run at 1 GPa.

Runs were initially taken to super liquidus conditions (Table 2) to ensure the homogeneity of the starting composition and promote growth of larger apatite crystals. Subsequently, the temperature was cooled isobarically to the final T at different rates (see Table 2). The final T and dwell time for each run (Table 2) was chosen to ensure apatite was the only phase present within the melt, allow equilibration between crystals and melt, and to also ensure apatite grains and areas of glass were a suitable size for analysis. On completion of the run samples were isobarically quenched by shutting off power to the heating circuit; T dropped to <50 °C in less than 30 seconds.

Oxygen fugacity was variably controlled in experiments by the sample environment. Initial runs were carried out using a single Pt capsule, which is assumed to have an oxygen fugacity in the vicinity of the Ni – NiO (NNO) solid buffer. Although fO_2 cannot be determined directly from the run products, it can be estimated by comparison with other experiments run using the same experimental procedure. In a separate series of experiments, run using the same bulk composition but doped with Eu, with the same sample preparation procedure and sample assembly, Eu XANES spectra indicate an Eu^{2+}/Eu^{3+} ratio in the melt phase close to that of the NNO buffer, as expected (Burnham et al. 2015).

A second suite of experiments were carried out using an inner graphite bucket inside a Pt capsule. As described by Médard et al. (2008), the presence of a graphite liner in the Pt capsule results in buffering of O by reaction with C, and more reducing conditions close to C - CO (CCO-1; Médard et al. 2008). Again, we cannot verify fO_2 conditions directly in these experiments, and it is possible that use of a Fe-free starting material here, for example, could result in slightly more reduced conditions than those described by Médard et al. (2008). However, it is unlikely that fO_2 conditions in graphite-Pt capsules will be more oxidising than CCO (Médard et al. 2008), providing a more reducing conditions than

samples run in just Pt or with an oxidising buffer. Oxygen fugacity in subsequent experiments was controlled using a double capsule technique (e.g., Eugster 1957; Eugster and Wones 1962; Jakobsson 2012). In these runs, fO_2 was controlled using a series of metal-metal oxide oxygen buffers (i.e. Ni-NiO, Cr-Cr_2O_3, Fe_3O_4-Fe_2O_3, Fe_3O_4-FeO) within an outer Pt capsule that enveloped an internal Pt capsule containing the starting material. Four µL of deionized (DI) water was micro-syringed into the bottom of all outer capsules regardless of starting composition prior to filing with the buffer and welding. In the $CaCl_2$ starting composition runs, 4µL of DI water was added into the inner capsule prior to filing and welding. Calculated oxygen fugacity values are given in Table 2 and were calculated based on the relevant redox buffer equations (Holzheid and O'Neill 1995, Jacobsson 1985, Médard et al. 2008, O'Neill 1988, O'Neill and Pownceby 1993). The fO_2 values for experiments run with a solid state buffer could deviate from the calculated buffer values if the activity of water inside the capsule is not in unity, and in water under-saturated samples, fO_2 values will be lower than the coexisting hydrated buffer (Matjuskin et al. 2015), and indicated in Table 2. The purpose of high-pressure experiments here, however, due to complexities in experimental design, is to synthesise apatite in equilibrium with silicate melt under a range of fO_2 conditions, from oxidising to reducing. Gas-mixing synthesis experiments are then used to accurately constrain the influence of fO_2 on Mn oxidation state.

Additional experiments were carried out in a vertical tube gas mixing furnace to synthesise Mn bearing glasses at controlled fO_2 conditions, at atmospheric pressure. A Mn-Fe doped granitic starting composition and a Mn doped granitic starting composition was mixed with poly-vinyl acetate (PVA) to create beads, each bead was hung on the end of a Pt loop. Multiple beads were organised on a chandelier and placed in the hot-spot of the furnace on the end of an alumina rod. Redox conditions inside the furnace were determined using CO_2-H_2 mixtures, with in line Bronkhorst mass flow controllers to regulate gas proportions as calculated using the tables of Deines (1970). All experiments were held at 1300 °C for 24 hours to equilibrate before being rapidly quenched by quickly raising the alumina rod out of the hot-spot.

1.4 *Analytical Techniques: EPMA*

Recovered capsules were mounted in crystal bond, ground to the desired level, and polished using diamond paste. Crystal bond was later dissolved using acetone. After cleaning, samples were mounted in 1" indium mounts and carbon coated. Glass beads from the gas mixing furnace experiments were embedded in epoxy, ground, and polished prior to analysis. Electron probe microanalysis data was collected using the JEOL JXA8530F Hyperprobe field emission gun electron microprobe analyser (FEG-EPMA) at the University of Bristol.

Apatite was analysed using a 10 µm beam for all conditions; the first protocol measured Na, Ca, P, F, and Cl with an accelerating voltage of 15keV and 5nA current. The second protocol used a 15 keV accelerating voltage and 20nA current to measure Si, Mg, K, S, Fe, Mn, Ni, Cr, and Ti on the same spot as the first protocol. Standards used were albite (Na, Si), Saint John's Island olivine (Mg), sanidine (K), barite (S), NaCl (Cl), fayalite (Fe), Mn metal (Mn), Ni metal (Ni), Cr_2O_3 (Cr), TiO_2 (Ti), and Durango apatite (Ca, P, F).

The glass was analysed with the following conditions: (1) 15keV accelerating voltage, 10nA current for Ca, Ti, Si, Al, Na, Mg, F, K, Cl, Fe and Ni (2) 15keV accelerating voltage, 40nA current for Mn, Cr, and P. All analyses were collected with a 10 µm beam and both protocols analysed the same spot. Standards were as follows: wollastonite (Ca), Saint John's Island olivine (Mg), TiO_2 (Ti), albite (Si, Na), MgF_2 (F), sanidine (Al, K), NaCl (Cl), fayalite (Fe, Mn), Cr_2O_3 (Cr), Durango apatite (P), and Ni metal (Ni).

1.5 Analytical Techniques: SIMS

Volatile measurements in the apatite and coexisting glasses were collected by secondary ion mass spectrometry (SIMS) on a Cameca ims-4f at the NERC ion probe facility at the University of Edinburgh. Prior to SIMS analysis samples were cleaned with ethanol, and then coated with ~35 nm gold to provide electrical conductivity.

Analyses were done using a $16O^-$ primary beam with nominal current of 2.2nA, and 10.8KeV accelerating voltage was targeted on a sample with a 4.5keV voltage to produce a ~15keV net impact energy. Apatite and glass measurements of the secondary ions 1H, 11B, 12C, 16O, 19F, 26Mg, 30Si, 31P, 35Cl, 39K, 42Ca, 55Mn, 88Sr, 138Ba, 139La, 140Ce and 151Eu were counted on an electron multiplier for 79 seconds respectively, for each 6 cycles of the magnet. A 3-minute pre-sputter period at a raster size of 10µm was used to pre-clean the analysis area. Secondary ions were acquired with a 25µm diameter image field, and the area analysed was restricted to 8-10µm spot size using a circular field aperture. An energy offset of 50eV was applied (40eV window). Higher resolution CO_2 measurements of glass and apatite were collected on additional spots (size permitting). These were acquired after a 4-minute pre sputter, with a 20µm raster, to pre clean the analysis area. Data was collected with a 60µm diameter image field, 50eV offset (40eV window), and a field aperture was used to restrict ions to a spot size of ~15µm in diameter. The mass resolution employed was 900-1000, which is sufficient to separate $25Mg^{2+}$ from $12C^+$. The majority of CO_2 measurements reported for apatite are based on the low-resolution window measurements, using higher resolution measurement to identify the need of an Mg correction. An Mg^{2+} correction based on $25Mg^{2+}$ was applied.

Only SIMS measurements for H_2O and CO_2 are given here, quantified by the 1H and 12C isotopes respectively. Other elements were measured to confirm that the analyses were not contaminated, and Eu/Ce measurements are for use in future investigation. Apatite standards (Bristol in-house standards – Riker et. al 2018) were used to quantify ion yields for 1H, and CO_2 analyses based on H/Ca and C/Ca ratios. Basaltic glass standards (ST-2 and ST-6) were used to quantify ion yields for 1H, and CO_2 analyses based on H/Si and C/Si . Absolute error for SIMS data is assumed to be better than 10%.

1.6 Analytical Techniques: XANES

Mn and Fe K-edge XANES spectra were collected on experimental capsules and glasses in 1” epoxy mounts at beamline I18 of the Diamond Light Source (Harwell, UK) in one three-day session. These samples were then removed from epoxy for subsequent analysis techniques (EPMA, SIMS). Spectra

were acquired in fluorescence mode, using a Ge detector. Beam energy was finely tuned using a Si(111) crystal monochromator. The beam size was selected by using a variety of slits and was focussed on an area of 5 µm × 5 µm. Mn K-edge scans were measured over an energy range of 6400-6750 eV with a 1s count time per point. The pre-edge region was measured in 5 eV steps from 6400-6520 eV and from 6520-6532 eV with 1 eV steps. The edge region from 6532-6562 eV was measured with 0.2 eV steps and 6562-6580 eV with 1 eV steps. The post-edge region was collected with 3 eV steps from 6600-6750 eV. Mn K-edge energy was calibrated by defining the first inflection point in the derivative of a Mn foil standard to 6539 eV.

Fe K-edge spectra were collected from 7000-7320 eV with a 1s count time per point. The pre-edge region was measured from 7000-7090 eV with 6.25 eV steps, and from 7090-7107 with 1 eV steps. The edge region was scanned with 0.25 eV steps from 7107-7120, 0.3eV steps from 7120-7140 eV and 1 eV steps over 7140-7160 eV. The post edge region from 7160-7320 was measured with 3 eV steps. Fe spectra energy was calibrated to the first inflection point in the derivative of a Fe foil standard to 7112 eV.

Multiple Fe and Mn XANES scans on a same sample were taken to check for a change in oxidation with beam exposure. Additional repeat scans were taken on the same sample but at additional spots at the start and end of the beamline session to check the reproducibility of the runs. No obvious shift in the pre-edge energy position was noted for spectra collected at the start and end of the session which is in fitting with the findings of Mosselmans et al. (2009), that the pre-edge position of Ti for scans taken 36 hours apart on beamline I18 shifted by ~0.03eV, which is less than the resolution of the beamline.

Raw data was imported into the software Athena (Ravel and Newville 2005), where multiple scan data was merged. Scans were also deglitched, corrected for self-absorption based on the FLUO algorithm (Haskel 1999) and then the data was pre-edge/post-edge normalised.

Pre-edge peak fitting was carried out on the normalised data in Fityk (Wojdyr 2010). Pre-edge peaks were obtained from the data by fitting a convex hull spline baseline across the pre-edge region.

228 Gaussian peaks of fixed half-width at half-maximum of 0.7 were fitted to the data. All data was fit
229 assuming two Gaussian contributions. The Gaussian contributions were used to calculate the average
230 integrated intensity for each fit, and was calculated from the sum of the integrated intensities of each
231 contributing peak. The 'average' centroid position was calculated from the area weighted centroid
232 positions of each Gaussian peak.

233 ## Experimental Results

234 All run products contained apatite and quenched melt (glass). In run PM1 H an additional unidentified
235 mineral phase was found. Apatite throughout the experiments varies in size from 2 to 500μm, in the
236 longest dimension, with the largest apatite found in the least silicic melts. Modal proportions of
237 apatite crystals are generally less than 30% and the habits of most crystals are euhedral. Apatite
238 commonly display elongate melt inclusions trapped in their cores, running parallel to the longest axis
239 of the crystals. Major, trace, and volatile measurements for glasses from each group of starting
240 compositions are listed in Table 2. Quenched glasses for all runs are homogenous in appearance and
241 have low standard deviation in major and minor element analyses. Apatites reveal no evidence of
242 chemical zonation. Furthermore, standard deviations for major and minor elements, calculated for
243 multiple analyses, are low (Table 3), and comparable to errors on individual analyses calculated by
244 JEOL software from counting statistics. This suggests that all our experiments are in equilibrium.

245 Glass compositions for runs with the PM1/Hap10 starting mix resulted in a range of compositions from
246 trachyte to phonotephroite/basaltic trachyandesite (Fig. 1). This range is due to varying degrees of
247 apatite saturation, and the additional effect of crystallising another phase in PM1 H. This also resulted
248 in different degrees of melt polymerisation as quantified by the ratio of non-bridging oxygens to
249 tetrahedrally coordinated cations (NBO/T). PM1 H contained the most polymerised melt upon
250 quenching (NBO/T = 0.12) and PM1 Pt the least (NBO/T = 0.43; Table 2), while the average NBO/T for
251 the PM1/Hap10 quenched glasses ≈ 0.26. MnO contents of the glasses vary from a minimum of 4.31
252 wt% in PM1 H to 9.21 wt% in PM1 Pt. Apatite from the PM1/Hap10 experiments has a range of Mn

contents from 4.94 wt% MnO (0.74 a.p.f.u. PM1 Pt) to 7.89 wt% MnO (1.16 a.p.f.u. - PM1 NNO), with an average of 6.51 wt% MnO. Molar proportion of Cl-H_2O for these apatite displays a range from more Cl rich (X^{Ap}_{Cl} = 0.89, PM1 Pt) in the PM1 samples to closer to pure hydroxyapatite compositions (X^{Ap}_{H2O} = 0.90, Cr 1200 Hap10) in HAP10 runs.

Sample Cr 1200 Hap5 was run in an additional starting composition (Table 1). Hap 5 is similar in composition to Hap10 but contained half the amount of Mn (5 wt.%). This experiment resulted in a trachyitic glass composition. Apatite in this run contained 6.58 wt% MnO (0.96 a.p.f.u.) and the anion content is close in composition to the hydroxyl end member (X^{Ap}_{H2O} = 0.85).

The SH3 composition resulted in glasses that are basaltic in composition, ranging from 4.00-4.32 wt% total alkalis (Na_2O + K_2O) and 45.42-46.47 wt% SiO_2 (Fig. 1). SH3 MH shows elevated FeO levels (1.75 wt% FeO) compared to other samples in this composition, presumably due to contamination from the buffer, occurring because of diffusion of Fe through the Pt into the sample. The MnO contents in these samples ranges from a minimum of 0.73 wt% MnO in SH3 Cr to a maximum of 0.90 wt% MnO in SH3 Pt. Apatite from this composition contains 0.90 wt% MgO (0.22 a.p.f.u.), and a maximum of 0.19 wt% MnO (0.03 a.p.f.u.). All apatite are close to the F end member composition with $X^{Ap}F$ ranging from 0.86-0.96 (Table 3).

Experiments run in the BMT2 system, with the exception of BMT2 MH, contain glasses that range from tephriphonolite to phonolite in composition (Fig. 1). Sample BMT2 MH was subject to Fe contamination from the buffer, with the addition of 12.1wt% FeO^T that changed the glass composition to a Fe-rich foidite (Fig. 1). The MnO content varied between 0.07-0.80 wt% in these quenched glasses, thought to be a result of differences in the amount of apatite crystallised. Apatite from this starting composition contained variable amounts of Mn compared to SH3, with 0.02, 0.04 and 0.07 a.p.f.u. of Mn for samples BMT2 Cr, MH and Pt respectively. BMT2 Cr is closest in composition to end member FAp (3.53 wt. %), whilst BMT2 Pt has the least amount of F (3.26 wt. %).

The compositions of 1 atm. gas mixing furnace glasses are given in Table 4. Both set of glasses are trachyitic in composition, with the exception of Fe-Mn granitic glasses Log fO_2 -5.1 and -6.3, which are tephriphonolite and trachyandesite, respectively. The Fe-Mn granitic glass Log fO_2 -6.3 is deficient in Na_2O and K_2O compared to the other samples. All samples were synthesised at the same temperature and left to dwell for the same time. Therefore, the difference in composition is likely to reflect a larger surface area to bead volume for this sample.

1.7 X-ray absorption near edge structure spectroscopy

X-ray absorption near edge structure (XANES) spectra were collected for the PM1 composition (samples NNO, Pt, PtC) to determine if any change in the oxidation state of Mn was detectable in samples synthesised under different fO_2 conditions. Sample PtC should be much more reduced (NNO-2.3, where NNO ± x refers to fO_2 relative to the Ni-NiO buffer in log 10 units), than both the Pt and NNO samples, which are both expected to be more oxidised, around NNO+0, even accounting for any uncertainties in the exact fO_2 at which samples were buffered. Spectra were obtained on both the quenched glass and apatite crystals to determine any change in Mn oxidation state. The XANES spectra from the quenched glass (Fig. 2) are remarkably similar in their shape, edge energy position and pre-edge peak energy position between samples PM1 NNO, Pt and PtC suggesting there is very little/no change in the oxidation state of Mn between these melts. When compared to tephroite (Mn_2SiO_4 – Mn^{2+}) and Mn_2O_3 (Mn^{3+}) standards, the edge position is very close to the tephroite standard suggesting Mn is in the 2+ oxidation state. There is no variation in the pre-edge peak position or intensity position (Table 5) for these glasses. This suggests no major change in oxidation state or Mn coordination between the quenched melts, with Mn incorporated exclusively, or almost exclusively, as Mn^{2+}.

XANES spectra for the PM1 apatite grains are also displayed in Figure 2. There are slight differences in these 3 spectra with the position of the edge crest varying from a minimum of 6551.33eV for PM1 Pt,

6551.75eV for PM1 PtC and 6553.947 eV for PM1 NNO. This shift is thought to represent a change in the local structure around Mn or an effect of crystal orientation (Dyar et al. 2002) rather than any systematic changes in Mn mean oxidation state. A change in oxidation state is unlikely, as no significant energy shift is observed in the pre-edge region (Table 5.), which is less sensitive to the environment of the absorbing atom (Chalmin et al. 2009). Apatite spectra also suggest no major change in Mn oxidation state between samples, with Mn dominantly present as Mn^{2+}.

Additional XANES spectra were collected on Mn and Fe-Mn doped glasses from the HAP10 composition, which were synthesised under carefully controlled oxygen fugacites (log fO_2 ranging from -9.4 to -0.7 at 1300 °C) in a gas-mixing furnace. Mn pre-edge peak spectra for the Mn K-edge of the glasses are shown in Figure 3A (Fe-Mn bearing glasses) and 3C (Mn glasses). Once again, there is no observable shift in the Mn pre-edge peak energy as a function of fO_2, suggesting that in all samples Mn is in a similar valence and environment. The position of the intensity averaged centroid and the location of the main edge suggest Mn^{2+} dominates in these silicate glasses. As there is no difference between the Fe-free and Fe-bearing Mn spectra, this suggests that there is no reduction or oxidation of the Mn^{3+} driven by redox changes in Fe during quench in the Fe-bearing samples. In contrast, the Fe K-edge pre-edge peaks obtained from the same glass samples (Fig. 3B), show a clear shift in pre-edge peak centroid to higher energy with more oxidising conditions. The oxidation state of Fe in the Fe bearing glasses has been determined using the variogram diagram from Fiege et al. (2017), which is based on the work of Wilke et al. (2001). Spectra collected on our glasses range from nearly 100% Fe^{2+} (samples 66 and 76) down to a minimum of 22.8% Fe^{2+} (sample air/100; Fig. 4), and are consistent with glasses in 5-fold, or a mix of 4- and 5-fold coordination.

Over the large range of fO_2-T space explored for the high pressure and 1 atm. glasses we have been unable to detect any measurable change in the oxidation state of Mn. XANES spectra instead imply that Mn^{2+} dominates in all samples. The average oxidation state of Mn in apatite appears not to change

as a function of fO_2-T conditions over the range of conditions used in this study. As such, we find no evidence to support the assertion that variation of fO_2 in magmas should result in any significant change in Mn valence.

Discussion

Oxygen fugacity and $D_{Mn}^{Ap\text{-}m}$

Our results demonstrate that the majority of Mn occurs as Mn^{2+} in melts across a range of fO_2 conditions. Here we test the empirical relationship defined by Miles et al. (2014; Fig. 5) by plotting $D_{Mn}^{Ap\text{-}m}$ (Nernst partition coefficient, $D_x = [x]_{mineral}/[x]_{melt,}$) as a function of fO_2. All samples in the SH3 haplo-basaltic composition show no significant variation in $D_{Mn}^{Ap\text{-}m}$ as a function of fO_2, even though there is a variation of approximately 17 log units in fO_2 between samples. Similarly, there is no obvious relationship between fO_2 and $D_{Mn}^{Ap\text{-}m}$ for PM1 and Hap10 melt compositions. This suggests that oxygen fugacity is not the main control on Mn apatite-melt partitioning in these compositions, although significant variation in Mn partitioning is noted for experiments involving different melt compositions. Samples in the BMT2 composition show an increase in $D_{Mn}^{Ap\text{-}m}$ with decreasing fO_2. This is unlikely to be due to changes in the availability of Mn^{2+} in the melt (i.e. due to imposed fO_2) as the XANES data indicates that the Mn^{2+}/Mn^{3+} ratio does not vary over a similar range in fO_2 to these experiments. Instead, the apparent fO_2 - $D_{Mn}^{Ap\text{-}m}$ trend for BMT2 coincidentally corresponds to changes in melt composition.

Melt polymerisation and $D_{Mn}^{Ap\text{-}m}$

It has long been recognised that trace element partition coefficients tend to be higher for minerals in equilibrium with more silicic melts (Blundy and Wood 2003). Although this may partly reflect disparity in the temperature and pressures of these systems it is thought the extent of melt polymerization is a key control on element partitioning (Mahood and Stimac 1990; Schmidt et al. 2006). Polymerisation is a measure of the extent to which silica tetrahedra within the melt structure are linked together. As

353 tetrahedral sites are linked together by shared oxygens (bridging oxygens), an increase in the extent
354 of polymerisation typically means a reduction in the ability of the melt to incorporate other elements.
355 Polymerisation of a melt can be compared in a variety of ways. In more felsic systems the aluminium
356 saturation index (ASI: molar ratio Al_2O_3/ (Na_2O+K_2O+CaO)) provides an indication of melt
357 polymerisation (Prowatke and Klemme 2005). However, the ratio of non-bridging oxygens (NBO) to
358 tetrahedrally coordinated cations (T) is becoming the standard indicator of melt polymerisation
359 (Cottrell et al. 2009). NBO/T = 0 represents a fully polymerized melt, whereas 4 represents a fully
360 depolymerised melt of isolated tetrahedral (Kohn and Schofield 1994). Here NBO/T was calculated
361 using the procedure originally documented by Mysen et al. (1982, 1984). All Fe has been assigned as
362 network modifiers, due to lack of information on Fe^{3+}/Fe^{T} in these samples.

363 Figure 6 displays the relationships between $D_{Mn}^{Ap\text{-}m}$ with NBO/T (Fig. 6A) and ASI (Fig. 6B) for samples
364 reported here and equivalent literature studies. ASI data from McCubbin et al. (2015) have not been
365 included given the absence of K_2O in their compositions. Both ASI and NBO/T parameters are
366 intrinsically linked, but there appears to be a stronger relationship between NBO/T and D_{Mn} than ASI,
367 indicating that melt polymerisation is more important than aluminosity in controlling Mn apatite-melt
368 partitioning. The partitioning of Mn into apatite in more polymerised melts appears to be considerably
369 greater than in more depolymerised melts, implying that melt structure has a strong influence on the
370 partitioning of Mn between apatite and melt. We would expect NBO/T to play a key role in dictating
371 $D_{Mn}^{Ap\text{-}m}$ over a range of melt compositions which are hosts of terrestrial apatite. Other parameters
372 which could influence $D_{Mn}^{Ap\text{-}m}$ are temperature and pressure. However, a similar relationship with
373 D_{Mn}/D_{Zn} (olivine-melt) and NBO/T was documented by Kohn and Schofield (1994), who also
374 demonstrated that melt composition has a stronger effect on mineral-melt partitioning than
375 temperature.

376 The relationship of NBO/T with $D_{Mn}^{Ap\text{-}m}$ may arise if Mn ions are coordinated with non-bridging
377 oxygens in silicate melts (Watson 1977). In more polymerised melts, the availability of non-bridging

oxygens is lower, and therefore, the extent to which melt networks incorporate metal cations such as Mn^{2+} will be reduced. Alternatively, the observed relationship can be explained based on Mn^{2+} interaction with melt networks, where Mn-O bonding in more polymerised melts is less favourable due to the destabilising effect it has on the silicate framework (Kohn and Schofield 1994). It is unlikely that the high $D_{Mn}^{Ap\text{-}m}$ are due to the octahedral site preference energy of the Mn^{2+} ion, as Mn^{2+} has an octahedral site preference energy of zero because of the ion's d^5 electron configuration (Kohn and Schofield 1994).

Mn content of apatite at Criffel pluton

Miles et al. (2014) highlighted that variations in the Mn content of apatite from different zones within the Criffell granitic pluton (southern Scotland) appeared to correlate with changes in melt fO_2, and were relatively independent of other parameters such as temperature and the concentration of Mn in the melt. As the partitioning data presented here indicates there is no relationship between $D_{Mn}^{Ap\text{-}m}$ and fO_2 we used the range of compositions from our study to test other hypotheses. If we apply the NBO/T to $D_{Mn}^{Ap\text{-}m}$ power relationship given in Figure 6 to the data for the Criffel pluton, we can determine apparent $D_{Mn}^{Ap\text{-}m}$ for the relevant melt compositions. NBO/T was calculated from whole rock compositions (Stephens and Halliday 1980; Miles et al. 2013) for the 4 petrologically distinct zones of the pluton for which apatite Mn concentrations were available (Miles et al. 2014). These compositions have been chosen to obtain the largest change in NBO/T. Whole rock MnO contents were combined with the modelled $D_{Mn}^{Ap\text{-}m}$ based on NBO/T to predict apatite MnO, and then data was converted to ppm for comparison. This method predicts a reasonable fit of the Mn apatite content (ppm) based on NBO/T with measured apatite concentrations from EPMA and SIMS data (Miles et al. 2014; Fig. 7). The error in Figure 7 is large indicating the sensitivity of apatite Mn content to the power law fit. The predicted Mn apatite content is also very sensitive to the modelled bulk rock composition and bulk rock MnO content. However, to a first approximation, it appears that the variation seen in apatite Mn concentration at Criffel can be explained solely by variations in NBO/T rather than fO_2. This

404 is, perhaps, unsurprising as XANES work indicates that over the range of fO_2 conditions inferred for
405 this pluton there is no change in the oxidation state of Mn^{2+} in silicate melt.

406

407 *Volatile partitioning as a function of melt structure and oxygen fugacity*
408

409 Manganese is unlikely to be the only element for which apatite-melt partitioning is affected by melt
410 composition. Aside from the effect which melt polymerisation should have on partitioning of other
411 cations readily incorporated onto octahedral sites in silicate melt structure, partitioning of anions
412 between apatite and melt may also be affected by NBO/T. Figure 8 shows that $D_{Cl}^{Ap\text{-}m}$ is also linked to
413 melt structure for dominantly hydroxyapatite compositions (X^{Ap}_{H2O} > 0.5 a.p.f.u.). In Figure 8, data
414 from this study as well as Doherty et al. (2014) and Prowatke and Klemme (2006), all show an increase
415 in $D_{Cl}^{Ap\text{-}m}$ with increasing polymerisation of the melt. This is similar to the trend noted for $D_{Mn}^{Ap\text{-}m}$, with
416 Cl becoming more incompatible in the melt with higher degrees of melt polymerisation. This may be
417 because the most polymerised melts also have lower wt% of Ca, Fe, Na and Mg, which are species
418 known to enhance the solubility of Cl in silicate melts (Mathez and Webster 2009).

419 It has been argued that Nernst partition coefficients are not suitable when examining the distribution
420 of halogens and water between apatite and melt (Boyce et al., 2014; McCubbin et al., 2015) as the
421 combined concentration of Cl, F and OH in the apatite structure is fixed based on stoichiometry
422 (McCubbin et al. 2015). A more suitable measure of volatile partitioning in apatite is the exchange
423 coefficient, K_D (Eq. 2). Equation 2 describes the exchange of OH-F between apatite and melt:

424 $$K_D^{OH-F} = \frac{\left(\frac{OH_{ap}}{OH_m}\right)}{\left(\frac{F_{ap}}{F_m}\right)} = \frac{\left(\frac{OH_{ap}}{F_{ap}}\right)}{\left(\frac{OH_m}{F_m}\right)} \quad [2]$$

425 The exchange coefficient allows partitioning behaviour of two major elements competing for the same
426 crystallographic site to be determined. The exchange coefficient treats F, Cl and H, as major elements,
427 and models them in a similar fashion to the behaviour of Mg and Fe between olivine and melt (Roeder

and Emslie 1970). Assuming ideal behaviour, K_D can be calculated using the mole fraction or wt. % of each species.

As such, instead of examining the relationship of $D_{Cl}^{Ap\text{-}m}$ with NBO/T, a more suitable parameter may be $K_D^{Cl\text{-}H2O}$. However, $K_D^{Cl\text{-}H2O}$ data from published literature for apatite of this composition is much more restricted, making it difficult to determine if there is a relationship with NBO/T.

In contrast, $D_F^{Ap\text{-}m}$ appears to be unaffected by melt composition for runs carried out in the fluorapatite end member composition, likely reflecting that F behaves slightly different in the melt structure to Cl, or that partitioning of F is more dependent on apatite crystal chemistry, and therefore less affected by melt composition.

Throughout the entire dataset there is no obvious influence of fO_2 on partitioning/exchange of the anions. Therefore, it is likely that mineral-melt partitioning of these elements is controlled by additional variables, such as, element availability in the melt, temperature, and structural controls from apatite and melt.

Conclusions

Apatite-silicate melt partitioning experiments described here demonstrate that fO_2 has no discernible influence on Mn or volatile partitioning. This is consistent with the results of XANES spectroscopy which demonstrate that over a wide range of fO_2 conditions Mn is incorporated into both apatite and a range of silicate melts as Mn^{2+}. Instead, results of this study, combined with literature data show that melt structure, and in particular the extent of melt polymerization as defined by the ratio NBO/T, controls partitioning of Mn between apatite and a range of silicate melts. The varying Mn content of apatite from the Criffel pluton can be explained by the varying degrees of melt polymerisation for samples from different zones of the pluton, rather than changes in the oxygen fugacity of the parental

magma, as previously suggested. More polymerised melts generally have a much higher mineral-melt partition coefficient for trace elements (e.g. Mn apatite-melt), than corresponding, less polymerised melts. Therefore, empirical relationships between variables such as oxygen fugacity and the Mn content in apatite are not valid across systems where melt composition changes, and further terms in such equations are needed to constrain the influence of melt composition.

Acknowledgements

The project was funded by the Natural Environment Research Council as part of a NERC E^3 DTP studentship (NERC grant NE/L002558/1), as well as analytical time at the NERC ion microprobe facility. Additional funding was granted from the Daniel Pidgeon fund – The Geological Society. XANES data was acquired at the Diamond Light Source, grant sp12876-1. We thank Stuart Kearns and Ben Buse for analytical support at the University of Bristol, and Richard Hinton for his expertise and guidance at the NERC ion microprobe facility. The authors thank Professor James Brenan, whose detailed review improved this manuscript.

References Cited

Belousova, E.A., Walters, S., Griffin, W.L., and O'Reilly, S.Y. (2001) Trace-element signatures of apatites in granitoids from the Mt Isa Inlier, northwestern Queensland. Australian Journal of Earth Sciences, 48, 603–619.

Blundy, J., and Wood, B. (2003) Partitioning of trace elements between crystals and melts. Earth and Planetary Science Letters, 210, 383–397.

Boyce, J.W., Tomlinson, S.M., McCubbin, F.M., Greenwood, J.P., and Treiman, A.H. (2014) The lunar apatite paradox. Science, 344, 400–402.

Brounce, M., Kelley, K.A., Cottrell, E., and Reagan, M.K. (2015) Temporal evolution of mantle wedge oxygen fugacity during subduction initiation. Geology, 43, 775–778.

Burnham, A. D., Berry, A. J., Halse, H. R., Schofield, P. F., Cibin, G., & Mosselmans, J. F. W. (2015). The

476 oxidation state of europium in silicate melts as a function of oxygen fugacity, composition and
477 temperature. Chemical Geology, 411, 248–259.

478 Cottrell, E., Walter, M. J., & Walker, D. (2009). Metal-silicate partitioning of tungsten at high pressure
479 and temperature: Implications for equilibrium core formation in Earth. Earth and Planetary
480 Science Letters, 281(3–4), 275–287.

481 Chalmin, E., Farges, F. & Brown, G.E. (2009). A pre-edge analysis of Mn K-edge XANES spectra to help
482 determine the speciation of manganese in minerals and glasses. Contribibutions to Mineralogy
483 and Petrology, 157, 111-126

484 Chu, M.-F., Wang, K.-L., Griffin, W.L., Chung, S.-L., O'Reilly, S.Y., Pearson, N.J., and Iizuka, Y. (2009)
485 Apatite Composition: Tracing Petrogenetic Processes in Transhimalayan Granitoids. Journal of
486 Petrology, 50, 1829.

487 Dai, L., and Karato, S. (2014) Influence of oxygen fugacity on the electrical conductivity of hydrous
488 olivine: Implications for the mechanism of conduction. Physics of the Earth and Planetary
489 Interiors, 232, 57–60.

490 Doherty, A. L., Webster, J. D., Goldoff, B. A., & Piccoli, P. M. (2014). Partitioning behavior of chlorine
491 and fluorine in felsic melt-fluid(s)-apatite systems at 50MPa and 850-950 °C. Chemical Geology,
492 384, 94–109.

493 Douce, A.E.P., and Roden, M. (2006) Apatite as a probe of halogen and water fugacities in the
494 terrestrial planets. Geochimica et Cosmochimica Acta, 70, 3173–3196.

495 Dyar, M. D., Gunter, M. E., Delaney, J. S., Lanzirotti, A., & Sutton, S. R. (2002). Use of the spindle
496 stage for orientation of single crystals for microXAS: Isotropy and anisotropy in Fe-XANES
497 spectra. American Mineralogist, 87(10), 1500–1504

498 Eugster, H. P. (1957). Heterogeneous Reactions Involving Oxidation and Reduction at High Pressures
499 and Temperatures. The Journal of Chemical Physics, 26(6), 1760–1761.

Eugster, H. P., & Wones, D. R. (1962). Stability Relations of the Ferruginous Biotite, Annite. Journal of Petrology, 3(1), 82–125.

Fiege, A., Ruprecht, P., Simon, A. C., Bell, A. S., Göttlicher, J., Newville, M., … Moore, G. (2017). Calibration of Fe XANES for high-precision determination of Fe oxidation state in glasses: Comparison of new and existing results obtained at different synchrotron radiation sources. American Mineralogist, 102(2), 369–380.

Fleet, M.E., Stone, W.E., and Crocket, J.H. (1991) Partitioning of palladium, iridium, and platinum between sulfide liquid and basalt melt: Effects of melt composition, concentration, and oxygen fugacity. Geochimica et Cosmochimica Acta, 55, 2545–2554.

Gross, J., Filiberto, J., and Bell, A.S. (2013) Water in the martian interior: Evidence for terrestrial MORB mantle-like volatile contents from hydroxyl-rich apatite in olivine–phyric shergottite NWA 6234. Earth and Planetary Science Letters, 369–370, 120–128.

Haskel, D. (1999). FLUO: Correcting XANES for self-absorption in fluorescence measurements.

Hensen, B.J. (1986) Theoretical phase relations involving cordierite and garnet revisited: the influence of oxygen fugacity on the stability of sapphirine and spinel in the system Mg-Fe-Al-Si-O. Contributions to Mineralogy and Petrology, 92, 362–367.

Holzheid, A., & O'Neill, H. S. C. (1995). The Cr-Cr_2O_3 oxygen buffer and the free energy of formation of Cr_2O_3 from high-temperature electrochemical measurements. Geochimica et cosmochimica acta, 59(3), 475-479.

Hughes, J.M. (2015) The many facets of apatite. American Mineralogist, 100, 1033–1039.

Hughes, J.M., Ertl, A., Bernhardt, H.-J., Rossman, G.R., and Rakovan, J. (2004) Mn-rich fluorapatite from Austria: Crystal structure, chemical analysis, and spectroscopic investigations. American Mineralogist, 89, 629–632.

523 Jacobsson, E. (1985). Solid State EMF Studies of the Systems FeO--Fe_3O_4 and Fe_3O_4--Fe_2O_3 in the
524 Temperature Range 1000-1600 K. Scandinavian Journal of Metallurgy., 14(5), 252-256.

525 Jakobsson, S. (2012). Oxygen fugacity control in piston-cylinder experiments. Contributions to
526 Mineralogy and Petrology, 164(3), 397–406

527 Kasting, J.F., Eggler, D.H., and Raeburn, S.P. (1993) Mantle Redox Evolution and the Oxidation State
528 of the Archean Atmosphere. The Journal of Geology, 101, 245–257.

529 Kohn, S.C., and Schofield, P.F. (1994) The importance of melt composition in controlling trace-
530 element behaviour: an experimental study of Mn and Zn partitioning between forsterite and
531 silicate melts. Chemical Geology, 117, 73–87.

532 Konecke, B.A., Fiege, A., Simon, A.C., Parat, F., and Stechern, A. (2017) Co-variability of S6+ , S4 + ,
533 and S2 – in apatite as a function of oxidation state : Implications for a new oxybarometer.
534 American Mineralogist, 102, 548–557.

535 Kump, L.R., Kasting, J.F., and Barley, M.E. (2001) Rise of atmospheric oxygen and the “upside-down”
536 Archean mantle. Geochemistry, Geophysics, Geosystems, 2, n/a--n/a.

537 Li, J., & Agee, C. B. (2001). The effect of pressure, temperature, oxygen fugacity and composition on
538 partitioning of nickel and cobalt between liquid Fe-Ni-S alloy and liquid silicate: Implications for
539 the Earth’s core formation. Geochimica et Cosmochimica Acta, 65(11), 1821–1832.

540 Mahood, G. A., & Stimac, J. A. (1990). Trace-element partitioning in pantellerites and trachytes.
541 Geochimica et Cosmochimica Acta, 54(8), 2257–2276.

542 Matjuschkin, V., Brooker, R. A., Tattitch, B., Blundy, J. D., & Stamper, C. C. (2015). Control and
543 monitoring of oxygen fugacity in piston cylinder experiments. Contributions to Mineralogy and
544 Petrology, 169(1), 9.

545 Marks, M. A. W., Scharrer, M., Ladenbuerger, S. and Markl, G.. Comment on ‘‘Apatite: A new redox

546 proxy for silicic magmas?" by Miles A.J., Graham C.M., Hawkesworth C., Gillespie M.R., Hinton
547 R.W., Bromiley G.D.. Geochim. Cosmochim. Acta (2016)

548 Mathez, E. A., & Webster, J. D. (2005). Partitioning behavior of chlorine and fluorine in the system
549 apatite-silicate melt-fluid. Geochimica et Cosmochimica Acta, 69(5), 1275–1286.

550 McCubbin, F.M., Vander Kaaden, K.E., Tartèse, R., Boyce, J.W., Mikhail, S., Whitson, E.S., Bell, A.S.,
551 Anand, M., Franchi, I.A., Wang, J., and others (2015) Experimental investigation of F, Cl, and OH
552 partitioning between apatite and Fe-rich basaltic melt at 1.0-1.2 GPa and 950-1000 °C.
553 American Mineralogist, 100, 1790–1802.

554 McCubbin, F.M., Boyce, J.W., Srinivasan, P., Santos, A.R., Elardo, S.M., Filiberto, J., Steele, A., and
555 Shearer, C.K. (2016) Heterogeneous distribution of H2O in the Martian interior: Implications for
556 the abundance of H2O in depleted and enriched mantle sources. Meteoritics and Planetary
557 Science, 51, 2036–2060.

558 Médard, E., McCammon, C.A., Barr, J.A., and Grove, T.L. (2008) Oxygen fugacity, temperature
559 reproducibility, and H2O contents of nominally anhydrous piston-cylinder experiments using
560 graphite capsules. American Mineralogist, 93, 1838–1844.

561 Miles, A. J., Graham, C. M., Hawkesworth, C. J., Gillespie, M. R., & Hinton, R. W. (2013). Evidence for
562 distinct stages of magma history recorded by the compositions of accessory apatite and zircon.
563 Contributions to Mineralogy and Petrology, 166(1), 1–19. https://doi.org/10.1007/s00410-013-
564 0862-9

565 Miles, A.J., Graham, C.M., Hawkesworth, C.J., Gillespie, M.R., Hinton, R.W., and Bromiley, G.D. (2014)
566 Apatite: A new redox proxy for silicic magmas? Geochimica et Cosmochimica Acta, 132, 101–
567 119.

568 Mosselmans, J. F. W., Quinn, P. D., Dent, A. J., Cavill, S. A., Moreno, S. D., Peach, A., Leicester, P. J.,
569 Keylock, S. J., Gregory, S. R., Atkinson, K. D. & Rosell, J. R. (2009). J. Synchrotron Rad. 16, 818-

824.

Moussallam, Y., Edmonds, M., Scaillet, B., Peters, N., Gennaro, E., Sides, I., and Oppenheimer, C. (2016) The impact of degassing on the oxidation state of basaltic magmas: A case study of Kīlauea volcano. Earth and Planetary Science Letters, 450, 317–325.

Mysen, B. O., Virgo, D., & Seifert, F. A. (1982). The structure of silicate melts: implications for chemical and physical properties of natural magma. Reviews of Geophysics, 20(3), 353-383.

Mysen, B. O., Virgo, D., & Seifert, F. A. (1984). Redox equilibria of iron in alkaline earth silicate melts; relationships between melt structure, oxygen fugacity, temperature and properties of iron-bearing silicate liquids. American Mineralogist, 69(9-10), 834-847.

Nagasawa, H. (1970) Rare earth concentrations in zircons and apatites and their host dacites and granites. Earth and Planetary Science Letters, 9, 359–364.

O'Neill, H. S. C. (1988). Systems Fe-O and Cu-O: thermodynamic data for the equilibria Fe-'FeO', Fe-Fe_3O_4,'FeO'-Fe_3O_4, Fe_3O_4-Fe_2O_3, Cu-Cu_2O, and Cu_2O-CuO from emf measurements. *Amer. Mineral*, *73*, 470-486.

O'Neill, H. S. C., & Pownceby, M. I. (1993). Thermodynamic data from redox reactions at high temperatures. I. An experimental and theoretical assessment of the electrochemical method using stabilized zirconia electrolytes, with revised values for the Fe-“FeO”, Co-CoO, Ni-NiO and Cu-Cu_2O oxygen buffers, and new data for the W-WO_2 buffer. Contributions to Mineralogy and Petrology, 114(3), 296-314.

Prowatke, S., and Klemme, S. (2005) Effect of melt composition on the partitioning of trace elements between titanite and silicate melt. Geochimica et Cosmochimica Acta, 69, 695–709.

Ravel, B., & Newville, M. (2005). ATHENA, ARTEMIS, HEPHAESTUS: data analysis for X-ray absorption spectroscopy using IFEFFIT. Journal of Synchrotron Radiation, 12(4), 537–541.

Riker, J., Humphreys, M. C. S., Brooker, R. A., & De Hoog, J. C. M. (2018). First measurements of OH-C

exchange and temperature-dependent partitioning of OH and halogens in the system apatite–silicate melt. American Mineralogist, 103(2), 260–270.

Roeder, P. L., and Emslie, R. (1970). Olivine-liquid equilibrium. Contributions to mineralogy and petrology, 29(4), 275-289.

Ryerson, F.J., Durham, W.B., Cherniak, D.J., and Lanford, W.A. (1989) Oxygen diffusion in olivine: Effect of oxygen fugacity and implications for creep. Journal of Geophysical Research: Solid Earth, 94, 4105–4118.

Scaillet, B., and Gaillard, F. (2011) Redox state of early magmas. Nature, 480, 48–49.

Schmidt, M. W., Connolly, J. A. D., Günther, D., & Bogaerts, M. (2006). Element partitioning: The role of melt structure and composition. Science, 312(5780), 1646–1650.

Scott, J.A.J., Humphreys, M.C.S., Mather, T.A., Pyle, D.M., and Stock, M.J. (2015) Insights into the behaviour of S, F, and Cl at Santiaguito Volcano, Guatemala, from apatite and glass. Lithos, 232, 375–394.

Sha, L.-K., and Chappell, B.W. (1999) Apatite chemical composition, determined by electron microprobe and laser-ablation inductively coupled plasma mass spectrometry, as a probe into granite petrogenesis. Geochimica et Cosmochimica Acta, 63, 3861–3881.

Shannon, R. D. (1976). Revised effective ionic radii and systematic studies of interatomic distances in halides and chalcogenides. Acta Crystallographica Section A, 32(5), 751–767.

Stephens, W.E., and Halliday, A.N. (1980) Discontinuities in the composition surface of a zoned pluton, Criffell, Scotland. GSA Bulletin, 91, 165–170.

Toplis, M.J., and Carroll, M.R. (1995) An Experimental Study of the Influence of Oxygen Fugacity on Fe-Ti Oxide Stability, Phase Relations, and Mineral—Melt Equilibria in Ferro-Basaltic Systems. Journal of Petrology, 36, 1137.

617 Trail, D., Watson, E.B., and Tailby, N.D. (2011) The oxidation state of Hadean magmas and
618 implications for early Earth's atmosphere. Nature, 480, 79–82.

619 Wallace, P., and Carmichael, I.S.E. (1992) Sulfur in basaltic magmas. Geochimica et Cosmochimica
620 Acta, 56, 1863–1874.

621 Watson, E. B. (1977). Partitioning of manganese between forsterite and silicate liquid. Geochimica et
622 Cosmochimica Acta, 41(9), 1363–1374.

623 Watson, E., Wark, D., Price, J., & Van Orman, J. (2002). Mapping the thermal structure of solid-
624 media pressure assemblies. Contributions to Mineralogy and Petrology, 142(6), 640–652.

625 Webster, J. D., Tappen, C. M., & Mandeville, C. W. (2009). Partitioning behavior of chlorine and
626 fluorine in the system apatite–melt–fluid. II: Felsic silicate systems at 200 MPa. Geochimica et
627 Cosmochimica Acta, 73(3), 559–581.

628 Wilke, M., Farges, F., Petit, P.-E., Brown, G. E., & Martin, F. (2001). Oxidation state and coordination
629 of Fe in minerals: An Fe K-XANES spectroscopic study. American Mineralogist, 86(5–6), 714–730

630 Wojdyr, M. (2010) Fityk: a general-purpose peak fitting program. Journal of Applied Crystallography,
631 43, 1126–1128.

632 Wood, B.J., and Nell, J. (1991) High-temperature electrical conductivity of the lower-mantle phase
633 (Mg, Fe)O. Nature, 351, 309.

634 Yang, X., Gaillard, F., & Scaillet, B. (2014). A relatively reduced Hadean continental crust and
635 implications for the early atmosphere and crustal rheology. Earth and Planetary Science
636 Letters, 393, 210–219.

637

638

639

640 **Figure captions**

641 **Figure 1:** Total alkali-silica (TAS) plot for quenched melt compositions. Sample names refer to oxygen
642 fugacity buffer and starting bulk composition used in each run, see text and table 2 for details.

643 **Figure 2: (A)** Stacked XANES spectra for PM1- Pt (solid green line), PtC (solid red line), and NNO glasses
644 (solid purple line) (B) focus on the pre-edge region of A. (C) Stacked XANES spectra of PM1- Pt (solid
645 green line), PtC (solid red line) and NNO (solid purple line) apatite (D) focus on pre-edge peaks of C.
646 Also plotted on A) and C) is an additional XANES spectrum of PM1 Pt with the spectra for the standards
647 tephroite (Mn_2SiO_4 - Mn^{2+}) (solid black line) and Mn_2O_3 (Mn^{3+}) (dashed black line).

648 **Figure 3:** (A) Mn K-edge, (B) Fe K-edge spectra acquired on the same set of Fe-Mn doped granitic glass,
649 and (C) Mn K-edge spectra from Mn doped granitic glass. For reference log fO_2 of NNO = -6.5 at 1300 °C.

650 **Figure 4**: Variogram (Wilke et al. 2001) that shows the average centroid position and integrated pre-
651 edge intensity for Fe reference compounds in single valence/single coordination (grey ellipses and
652 black dots). The black dotted lines indicate binary mixes between the end member reference
653 compounds. Also plotted are the centroid position and intensity for the Fe-Mn doped granitic glasses
654 from this study (crosses). For reference log fO_2 of NNO = -6.5 at 1300 °C.

655 **Figure 5:** $D_{Mn}^{Ap\text{-}m}$ plotted as a function of log fO_2 for apatite-melt partitioning experiments from this
656 study.

657 **Figure 6:** $D_{Mn}^{Ap\text{-}m}$ plotted as a function of ASI (Aluminium saturation index) and NBO/T (number of
658 nonbridging oxygen per tetrahedral cation) for samples in this study and those from Sha and Chappell
659 (1999), Belousova et al. (2001), and McCubbin et al. (2015). The power fit is fitted using data from this
660 study, McCubbin et al. (2015) and Sha and Chappell (1999). Belousova et al. (2001) data is not used
661 for the power law fit because although the data shows a similar trend to other studies, there is an
662 unexplained offset to lower NBO/T.

663 **Figure 7:** Boxplot of Mn apatite concentration (ppm) for the 4 petrologically distinct zones of the Criffel
664 Pluton (Miles et al. 2014). The blue box highlights the interquartile range for the dataset, with the blue
665 line indicating the median value. The black whiskers represent the range of the dataset. Overlaying
666 this data is the apparent Mn apatite concentration (red crosses) determined from the power law
667 relationship between NBO/T and $D_{Mn}^{Ap\text{-}m}$ shown in Fig. 6, and associated error (red lines) based on the
668 90% confidence intervals.

669 **Figure 8:** $D_{Cl}^{Ap\text{-}m}$ against melt NBO/T for our study and literature data (Mathez and Webster 2005;
670 Webster et al. 2009; Doherty et al. 2014).

671

Table 1: Target melt compositions, wt% oxide, without additional apatite component. Added to each bulk composition was a 7:3 of starting material to apatite component, consisting of 1.5 mol $Ca_3(PO_4)_2$ to either 1 mol. $CaCl_2$ (PM1/HAP10/HAP5) or 1 mol. CaF_2 (BMT2/SH3). H_2O added in the form of brucite or gibbsite

	PM1	HAP10	HAP5	BMT2	SH3
SiO_2	64.1	63.7	72.2	61.3	52.2
TiO_2	-	-	-	0.4	-
Al_2O_3	17.1	17.1	13.4	18.4	17.3
FeO	-	-	-	3.1	-
MnO	7.4	7.3	5.3	1.0	1.0
MgO	-	-	-	0.2	11.5
CaO	-	-	-	0.9	12.1
Na_2O	4.7	4.7	5.4	6.1	2.7
K_2O	6.8	7.2	3.7	7.0	1.8
H_2O*	-	-	-	1.5	1.5

Table 2: Experimental parameters, and average major and trace element composition of melt for experimental runs. Errors represent 1σ. Duration relates to hours at final T, while ramp rate is degrees cooled per hour. Note: Pt = single Pt capsule, H= single Pt capsule with added H_2O, NNO = Ni-NiO buffer, MH = Fe_3O_4-Fe_2O_3 buffer, MW = Fe_3O_4-FeO buffer, Cr = Cr-Cr_2O_3 buffer, PtC = graphite capsule inside Pt. H_2O measurements were made by SIMS. NBO/T = number of non-bridging oxygen per tetrahedrally coordinated cation (see text for details).

	PM1 Pt	PM1 H	PM1 NNO	PM1 PtC	MH 1200 Hap10	MW 1200 Hap10	Cr 1200 Hap10	NNO 1200 Hap10	Cr 1200 Hap5
Initial T	1450	1450	1450	1450	1400	1400	1400	1400	1400
Final T	1250	1100	1250	1250	1200	1200	1200	1200	1200
Ramp Rate	60	60	60	60	60	60	60	60	60
Est. fO_2[1]	-7.0	-8.8	-7.0	-9.9	-2.9	-9.3	-17.6	-7.6	-17.6
Duration	23	18	20	21	19	20	24	21	21
Glass									
SiO_2	53.39 ± 0.64	61.86 ± 0.78	52.38 ± 0.38	56.13 ± 0.68	50.07 ± 0.58	56.89 ± 1.11	53.48 ± 0.41	52.13 ± 0.51	63.00 ± 0.85
TiO_2									
Al_2O_3	14.40 ± 0.18	17.85 ± 0.27	15.51 ± 0.20	16.08 ± 0.18	14.60 ± 0.16	16.11 ± 0.17	15.18 ± 0.15	15.41 ± 0.41	12.93 ± 0.13
FeO^T					1.66 ± 0.12	1.57 ± 0.09	0.03 ± 0.01		
MgO					0.10 ± 0.01	0.25 ± 0.02	0.07 ± 0.01	0.08 ± 0.01	0.08 ± 0.01
MnO	9.21 ± 0.52	4.31 ± 0.34	9.06 ± 0.32	6.69 ± 0.27	7.57 ± 0.31	7.16 ± 0.53	7.18 ± 0.22	7.65 ± 0.33	3.88 ± 0.03
CaO	6.10 ± 0.27	1.71 ± 0.08	4.56 ± 0.11	4.43 ± 0.13	4.05 ± 0.19	3.27 ± 0.29	3.32 ± 0.09	4.61 ± 0.23	2.58 ± 0.08
K_2O	5.14 ± 0.13	6.67 ± 0.10	4.45 ± 0.07	4.85 ± 0.1	5.20 ± 0.10	6.22 ± 0.16	5.54 ± 0.12	5.47 ± 0.13	3.48 ± 0.08
Na_2O	5.21 ± 0.14	5.45 ± 0.07	2.51 ± 0.09	3.38 ± 0.13	3.32 ± 0.19	4.03 ± 0.12	3.68 ± 0.26	3.68 ± 0.25	4.57 ± 0.13
P_2O_5	3.46 ± 0.23	0.82 ± 0.07	2.85 ± 0.12	1.76 ± 0.11	3.62 ± 0.40	2.12 ± 0.08	2.70 ± 0.20	3.41 ± 0.32	2.20 ± 0.02
Cl	2.45 ± 0.13	0.47 ± 0.03	0.29 ± 0.03	2.08 ± 0.11	0.46 ± 0.01	0.22 ± 0.01	0.15 ± 0.00	0.56 ± 0.05	0.08 ± 0.01
F									
Total	99.35 ± 0.29	99.14 ± 0.99	91.6 ± 0.48	95.39 ± 0.52	90.71 ± 0.89	97.91 ± 0.45	91.39 ± 0.39	93.27 ± 0.87	92.93 ± 0.89
H_2O	0.92		7.79	2.78	7.97		7.63	5.60	6.44
CO_2	0.16		0.11	0.03				0.20	
NBO/T	0.43	0.12	0.27	0.21	0.29	0.24	0.25	0.30	0.15

Table 2 continued

	SH3 Cr	SH3 PtC	SH3 Pt	SH3 MH	BMT2 Cr	BMT2 Pt	BMT2 MH
Initial T	1400	1400	1400	1400	1500	1500	1500
Final T	1250	1250	1250	1250	1350	1350	1350
Ramp Rate	60	60	60	60	10	10	10
Est. fO_2[1]	-16.76	-9.91	-7.00	-2.32	-15.20	-6.00	-1.28
Duration	24	24	24	24	9	9	9
Glass							
SiO_2	46.47 ± 0.43	46.36 ± 0.45	45.78 ± 0.43	45.42 ± 0.50	60.56 ± 0.45	55.80 ± 0.63	45.38 ± 0.49
TiO_2					0.27 ± 0.04	0.30 ± 0.02	0.25 ± 0.01
Al_2O_3	15.64 ± 0.18	15.59 ± 0.18	15.47 ± 0.01	15.33 ± 0.11	18.45 ± 0.09	17.49 ± 0.09	13.34 ± 0.21
FeO^T		0.04 ± 0.01		1.75 ± 0.05		1.29 ± 0.05	12.08 ± 0.20
MgO	10.00 ± 0.07	10.18 ± 0.06	10.00 ± 0.05	8.55 ± 0.07	0.32 ± 0.01	0.30 ± 0.01	0.28 ± 0.01
MnO	0.73 ± 0.02	0.79 ± 0.02	0.90 ± 0.01	0.86 ± 0.01	0.07 ± 0.01	0.76 ± 0.01	0.58 ± 0.01
CaO	16.47 ± 0.20	16.46 ± 0.06	16.16 ± 0.30	15.56 ± 0.05	3.60 ± 0.03	4.31 ± 0.12	8.11 ± 0.13
K_2O	1.58 ± 0.05	1.58 ± 0.06	1.49 ± 0.05	1.66 ± 0.02	6.97 ± 0.09	6.27 ± 0.08	5.09 ± 0.08
Na_2O	2.62 ± 0.13	2.42 ± 0.14	2.51 ± 0.17	2.66 ± 0.14	6.34 ± 0.17	5.73 ± 0.26	4.76 ± 0.26
P_2O_5	4.15 ± 0.12	3.99 ± 0.03	4.19 ± 0.01	4.03 ± 0.02	1.35 ± 0.05	2.48 ± 0.08	5.74 ± 0.18
Cl							
F	1.35 ± 0.05	1.36 ± 0.05	1.37± 0.03	1.28 ± 0.08	1.00 ± 0.06	1.07 ± 0.08	1.22 ± 0.07
Total	99.07 ± 0.48	98.78 ± 0.45	97.90 ± 0.20	97.11 ± 0.65	99.09 ± 0.25	95.78 ± 0.37	96.88 ± 0.51
H_2O	1.60	0.89	1.89	1.89	0.48	2.07	1.90
CO_2	0.69	0.29					
NBO/T	0.86	0.86	0.86	0.79	0.11	0.15	0.36

[1]fO_2 estimated based on a_{H2O}=1; for all double capsule experiments it is possible that fO_2 is lower due to reduced a_{H2O}.

Table 3: Major and trace element compositions of apatite, and associated partition coefficients for experimental runs. Errors represent 1σ. Note: Pt = single Pt capsule, H= single Pt capsule with added H_2O, NNO =Ni-NiO buffer, MH = Fe_3O_4-Fe_2O_3 buffer, MW = Fe_3O_4-FeO buffer,Cr = Cr-Cr_2O_3 buffer, PtC = graphite capsule inside Pt. H_2O measurements were made by SIMS. $X^{Ap}F = F^{Ap}/3.767$, $X^{Ap}Cl = Cl^{Ap}/6.809$ and $X^{Ap}H2O = H_2O^{Ap}/1.81$. Structural formulas are calculated based on 26 anions.

	PM1 Pt	PM1 H	PM1 NNO	PM1 C	MH 1200 Hap10
# Analyses	17	20	28	19	9
SiO_2	0.37 ± 0.06	0.48 ± 0.10	0.27 ± 0.05	0.45 ± 0.05	0.18 ± 0.01
Al_2O_3	0.04 ± 0.01	0.06 ± 0.02		0.06 ± 0.03	
FeO^T					0.14 ± 0.04
MgO					
MnO	4.94 ± 0.15	6.6 ± 0.25	7.89 ± 0.28	5.93 ± 0.24	5.67 ± 0.50
CaO	48.28 ± 0.24	46.93 ± 0.37	47.51 ± 0.35	47.34 ± 0.49	49.23 ± 0.46
K_2O	0.14 ± 0.03	0.19 ± 0.05	0.07 ± 0.03	0.13 ± 0.02	0.02 ± 0.00
Na_2O	0.59 ± 0.04	0.60 ± 0.05	0.06 ± 0.03	0.33 ± 0.04	0.13 ± 0.03
P_2O_5	39.89 ± 0.46	39.81 ± 0.27	40.5 ± 0.47	39.7 ± 0.63	40.83 ± 0.49
Cl	6.03 ± 0.38	5.20 ± 0.60	0.94 ± 0.05	5.79 ± 0.91	1.15 ± 0.02
F					
Total	100.27 ± 0.64	99.87 ± 0.62	97.28 ± 0.51	99.72 ± 0.65	97.11 ± 0.39
H_2O	0.09		1.40	0.17	1.43
CO_2	0.08		0.07	0.04	0.06
Al	0.01	0.01		0.01	
Fe					0.02
Mg					
Mn	0.74	0.99	1.16	0.89	0.83
Ca	9.12	8.86	8.84	8.99	9.12
K	0.06	0.09	0.03	0.06	0.01
Na	0.20	0.21	0.02	0.11	0.04
Sum Ca Site	10.13	10.15	10.06	10.06	10.03
P	5.95	5.94	5.96	5.95	5.98
Si	0.05	0.07	0.04	0.07	0.03
Sum P site	6.00	6.01	6.00	6.02	6.01
Cl	1.80	1.55	0.28	1.74	0.34
F					
H_2O	0.11		1.62	0.20	1.65
Sum X site	1.91		1.90	1.94	1.99
$X^{Ap}Cl$	0.89		0.14	0.85	0.17
$X^{Ap}F$					
$X^{Ap}H_2O$	0.05		0.77	0.09	0.79
X^{Ap}total	0.94		0.91	0.94	0.96
$D_{Mn}^{ap/m}$	0.54	1.53	0.87	0.89	0.75
$D_{H2O}^{ap/m}$	0.10		0.18	0.06	0.18
$K_D^{Cl\text{-}H2O}$	21.18		0.22	5.30	0.21
$K_{DF}^{F\text{-}H2O}$					

Table 3 continued

	MW 1200 Hap10	Cr 1200 Hap10	NNO 1200 Hap10	Cr 1200 Hap5
# Analyses	4	8	7	6
SiO_2	0.55 ± 0.23	0.23 ± 0.02	0.27 ± 0.02	0.27 ± 0.02
Al_2O_3				
FeO^T	0.67 ± 0.12			
MgO	0.15 ± 0.01	0.03 ± 0.00		0.06 ± 0.01
MnO	7.14 ± 0.49	7.30 ± 0.61	6.61 ± 0.06	6.58 ± 0.08
CaO	46.57 ± 0.66	47.76 ± 0.57	48.11 ± 0.21	48.24 ± 0.22
K_2O	0.11 ± 0.04	0.06 ± 0.02	0.05 ± 0.01	0.04 ± 0.01
Na_2O	0.28 ± 0.03	0.08 ± 0.02	0.19 ± 0.03	0.18 ± 0.07
P_2O_5	40.24 ± 0.59	40.92 ± 0.56	40.51 ± 0.50	41.21 ± 0.29
Cl	1.89 ± 0.10	0.63 ± 0.04	1.93 ± 0.03	0.74 ± 0.05
F	0.24 ± 0.30			
Total	97.86 ± 0.60	96.73 ± 0.65	97.41 ± 0.64	97.15 ± 0.27
H_2O		1.63	1.35	1.54
CO_2		0.08	0.11	0.08
Al				
Fe	0.10			
Mg	0.04	0.01		0.02
Mn	1.06	1.07	0.97	0.96
Ca	8.71	8.85	8.98	8.90
K	0.05	0.03	0.02	0.02
Na	0.09	0.03	0.06	0.06
Sum Ca Site	10.05	9.98	10.04	9.95
P	5.95	5.99	5.97	6.01
Si	0.08	0.03	0.04	0.04
Sum P site	6.03	6.02	6.01	6.04
Cl	0.56	0.18	0.57	0.22
F	0.13			
H_2O		1.88	1.57	1.77
Sum X site		2.07	2.14	1.98
$X^{Ap}Cl$		0.09	0.28	0.11
$X^{Ap}F$				
$X^{Ap}H_2O$		0.90	0.75	0.85
X^{Ap}total		0.99	1.03	0.96
$D_{Mn}^{ap/m}$	1.00	1.02	0.86	1.70
$D_{H2O}^{ap/m}$		0.21	0.24	0.24
$K_D^{Cl\text{-}H2O}$		0.28	0.40	0.90
$K_{DF}^{F\text{-}H2O}$				

Table 3 continued

	SH3 Cr	SH3 PtC	SH3 Pt	SH3 MH
# Analyses	5	6	4	8
SiO_2	0.39 ± 0.05	0.42 ± 0.06	0.39 ± 0.10	0.39 ± 0.10
Al_2O_3				
FeO^T				0.05 ± 0.04
MgO	0.88 ± 0.01	0.86 ± 0.02	0.90 ± 0.01	0.87 ± 0.02
MnO	0.16 ± 0.01	0.19 ± 0.01	0.18 ± 0.01	0.19 ± 0.02
CaO	54.3 ± 0.18	53.96 ± 0.23	54.51 ± 0.10	54.36 ± 0.45
K_2O		0.02 ± 0.01		0.02 ± 0.01
Na_2O				
P_2O_5	41.28 ± 0.67	41.79 ± 0.48	41.39 ± 0.22	41.71 ± 0.39
Cl	0.02 ± 0.02	0.04 ± 0.01	0.03 ± 0.01	0.02 ± 0.02
F	3.24 ± 0.19	3.34 ± 0.12	3.61 ± 0.31	3.25 ± 0.18
Total	100.33 ± 0.58	100.71 ± 0.31	101.06 ± 0.19	100.92 ± 0.44
H_2O	0.37	0.26	0.20	0.40
CO_2	0.28	0.21	0.43	0.24
Al				
Fe				0.01
Mg	0.22	0.22	0.23	0.22
Mn	0.02	0.03	0.03	0.03
Ca	9.85	9.74	9.86	9.79
K		0.01		0.01
Na				
Sum Ca Site	10.10	9.99	10.11	10.05
P	5.92	5.96	5.91	5.94
Si	0.05	0.06	0.05	0.05
Sum P site	5.97	6.02	5.97	5.99
Cl	0.01	0.01	0.01	0.01
F	1.74	1.78	1.93	1.73
H_2O	0.42	0.29	0.23	0.45
Sum X site	2.16	2.08	2.16	2.18
$X^{Ap}Cl$		0.01		
$X^{Ap}F$	0.86	0.89	0.96	0.86
$X^{Ap}H_2O$	0.20	0.14	0.11	0.22
X^{Ap}total	1.07	1.04	1.07	1.09
$D_{Mn}^{ap/m}$	0.22	0.24	0.20	0.22
$D_{H2O}^{ap/m}$	0.23	0.30	0.11	0.21
K_D^{Cl-H2O}				
K_{DF}^{F-H2O}	4.38	3.21	9.90	4.43

37

38

	BMT2 Cr	BMT2 Pt	BMT2 MH
# Analyses	4	7	5
SiO_2	0.32 ± 0.11	0.17 ± 0.01	0.17 ± 0.02
Al_2O_3			
FeO^T		0.14 ± 0.02	0.61 ± 0.03
MgO	0.12 ± 0.01	0.10 ± 0.01	0.07 ± 0.00
MnO	0.15 ± 0.04	0.49 ± 0.06	0.27 ± 0.01
CaO	54.64 ± 0.45	54.44 ± 0.15	54.40 ± 0.23
K_2O	0.09 ± 0.04	0.06 ± 0.02	0.05 ± 0.01
Na_2O	0.11 ± 0.03	0.08 ± 0.02	0.09 ± 0.05
P_2O_5	41.47 ± 0.36	41.52 ± 0.52	41.82 ± 0.42
Cl			0.02 ± 0.02
F	3.53 ± 0.21	3.26 ± 0.13	3.40 ± 0.12
Total	100.5 ± 0.47	100.28 ± 0.50	100.94 ± 0.34
H_2O	0.16	0.26	0.36
CO_2	0.15	0.21	0.09
Al			
Fe		0.02	0.09
Mg	0.03	0.03	0.02
Mn	0.02	0.07	0.04
Ca	9.93	9.90	9.84
K	0.04	0.03	0.02
Na	0.04	0.03	0.03
Sum Ca Site	10.06	10.07	10.03
P	5.96	5.96	5.98
Si	0.05	0.02	0.02
Sum P site	6.00	5.99	6.00
Cl			0.01
F	1.89	1.75	1.82
H_2O	0.18	0.29	0.41
Sum X site	2.07	2.04	2.23
$X^{Ap}Cl$			
$X^{Ap}F$	0.94	0.87	0.90
$X^{Ap}H_2O$	0.09	0.14	0.20
X^{Ap}total	1.03	1.01	1.10
$D_{Mn}^{ap/m}$	2.14	0.65	0.47
$D_{H2O}^{ap/m}$	0.34	0.16	0.19
$K_D^{Cl\text{-}H2O}$			
$K_{DF}^{F\text{-}H2O}$	6.50	14.39	7.94

39

Table 4: Major element compositions of Mn granitic and Fe-Mn granitic glasses synthesised in a 1 atm. Gas mixing furnace under reducing conditions. Errors represent 1σ.

A - Mn granitic glasses

Log fO_2	-0.7	<-4	-5.1	-6.3	-7.8	-8.9	-9.4
SiO_2	61.20 ± 1.22	62.40 ± 1.04	61.66 ± 0.54	62.01 ± 0.73	60.76 ± 1.27	62.85 ± 1.70	63.48 ± 0.55
Al_2O_3	19.06 ± 0.39	17.64 ± 0.52	17.89 ± 0.66	18.07 ± 0.29	18.61 ± 0.70	17.62 ± 0.91	17.93 ± 0.10
FeO^T							
MnO	8.64 ± 0.75	8.70 ± 0.58	9.26 ± 0.35	9.25 ± 0.34	9.23 ± 0.42	9.29 ± 0.93	6.55 ± 0.80
K_2O	6.68 ± 0.18	6.80 ± 0.18	6.81 ± 0.07	6.82 ± 0.14	6.59 ± 0.15	6.39 ± 0.12	7.10 ± 1.25
Na_2O	4.83 ± 0.08	4.73 ± 0.17	4.75 ± 0.10	4.64 ± 0.07	4.58 ± 0.09	4.14 ± 0.12	4.38 ± 0.74
Total	100.54 ± 0.69	100.37 ± 0.45	100.48 ± 1.12	100.90 ± 0.32	99.88 ± 0.61	100.41 ± 0.53	99.56 ± 0.80

B - Mn-Fe granitic glasses

Log fO_2	-0.7	<-4	-5.1	-6.3	-7.8	-8.9	-9.4
SiO_2	59.67 ± 1.37	60.62 ± 1.19	57.00 ± 0.75	61.28 ± 1.34	60.41 ± 2.26	61.33 ± 0.86	61.10 ± 2.03
Al_2O_3	19.36 ± 0.90	18.08 ± 0.97	18.43 ± 0.13	18.56 ± 0.66	17.78 ± 0.60	16.95 ± 0.26	17.75 ± 0.52
FeO^T	4.81 ± 0.17	5.40 ± 0.11	7.61 ± 0.17	8.43 ± 0.66	6.65 ± 0.97	7.05 ± 0.25	6.06 ± 0.89
MnO	3.91 ± 0.36	3.58 ± 0.27	4.38 ± 0.11	4.13 ± 0.35	3.75 ± 0.58	3.64 ± 0.12	3.48 ± 0.53
K_2O	6.96 ± 0.19	7.02 ± 0.08	6.78 ± 0.07	3.88 ± 0.22	6.71 ± 0.23	6.76 ± 0.11	7.01 ± 0.21
Na_2O	5.02 ± 0.11	4.88 ± 0.13	4.83 ± 0.20	3.16 ± 0.12	4.57 ± 0.10	4.38 ± 0.16	4.39 ± 0.12
Total	99.76 ± 0.41	99.60 ± 0.52	99.07 ± 0.51	99.48 ± 0.24	99.90 ± 0.50	100.14 ± 0.55	99.80 ± 0.41

42 **Table 5:** Pre edge peak fitting for PM1 Pt, PM1 PtC and PM1 NNO. Apt = apatite.

43

Sample	Centroid (eV)	Intensity
PM1 Pt Glass	6540.46	0.078
PM1 PtC Glass	6540.43	0.080
PM1 NNO Glass	6540.46	0.071
PM1 Pt Apt.	6540.44	0.064
PM1 PtC Apt.	6540.44	0.063
PM1 NNO Apt.	6540.49	0.054

44

Table 6: Whole rock geochemistry for thought to be representative of the four petrologic zones at the Criffel Pluton. [1]Values from (Miles et al., 2013. [2]Values from (Stephens & Halliday, 1980).

	Zone 1 (09-17)[1]	Zone 2 (09-18)[1]	Zone 3 (09-21)[1]	Zone 4 (274)[2]
SiO_2	63.92	66.04	69.52	71.35
TiO_2	0.58	0.53	0.36	0.21
Al_2O_3	15.75	15.33	15.10	15.39
FeO^T	3.24	2.74	1.89	1.33
MnO	0.06	0.05	0.04	0.04
MgO	2.51	1.97	0.93	0.97
CaO	3.82	2.67	2.02	0.90
K_2O	3.35	3.86	4.20	4.70
Na_2O	4.12	3.99	3.84	3.84
P_2O_5	0.29	0.26	0.17	0.10
NBO/T	0.18	0.13	0.06	0.03

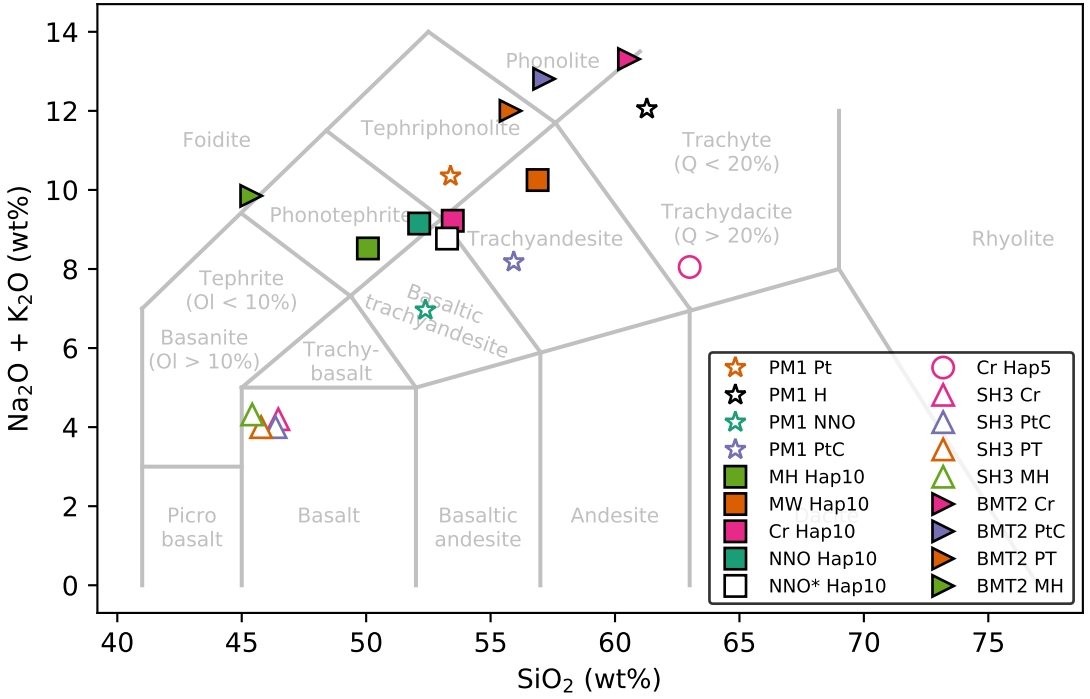
Phonolite
Foidite
Tephriphonolite
Trachyte
(Q < 20%)
Trachydacite
(Q > 20%)
Rhyolite
Phonotephrite
Trachyandesite
Tephrite
(Ol < 10%)
Basaltic
trachyandesite
Basanite
(Ol > 10%)
Trachy-
basalt
Picro
basalt
Basalt
Basaltic
andesite
Andesite
Dacite
PM1 Pt
PM1 H
PM1 NNO
PM1 PtC
MH Hap10
MW Hap10
Cr Hap10
NNO Hap10
NNO* Hap10
Cr Hap5
SH3 Cr
SH3 PtC
SH3 PT
SH3 MH
BMT2 Cr
BMT2 PtC
BMT2 PT
BMT2 MH
Na2O + K2O (wt%)
SiO2 (wt%)
0
2
4
6
8
10
12
14
40
45
50
55
60
65
70
75

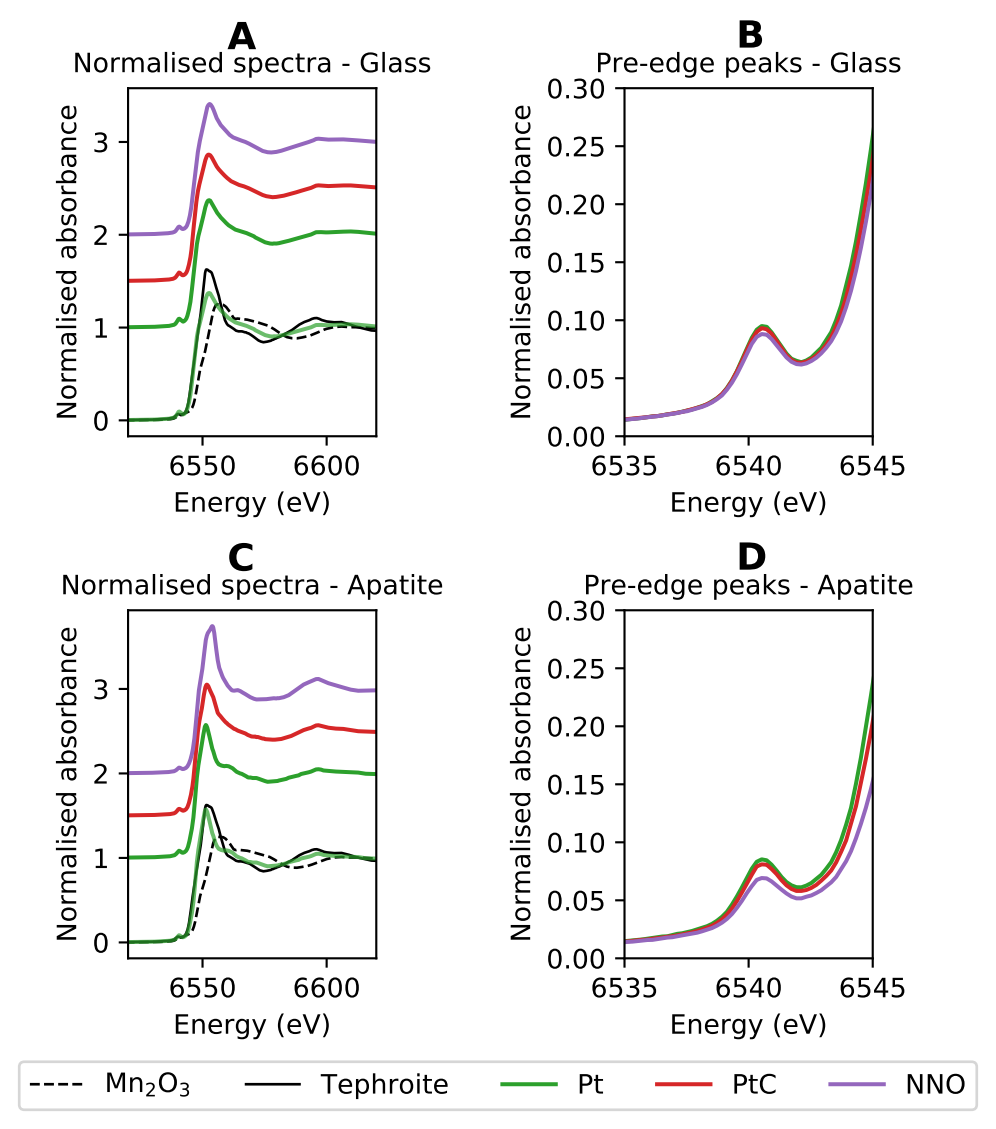
A
Normalised spectra - Glass
Normalised absorbance
Energy (eV)
B
Pre-edge peaks - Glass
Normalised absorbance
Energy (eV)
C
Normalised spectra - Apatite
Normalised absorbance
Energy (eV)
D
Pre-edge peaks - Apatite
Normalised absorbance
Energy (eV)
Mn2O3
Tephroite
Pt
PtC
NNO

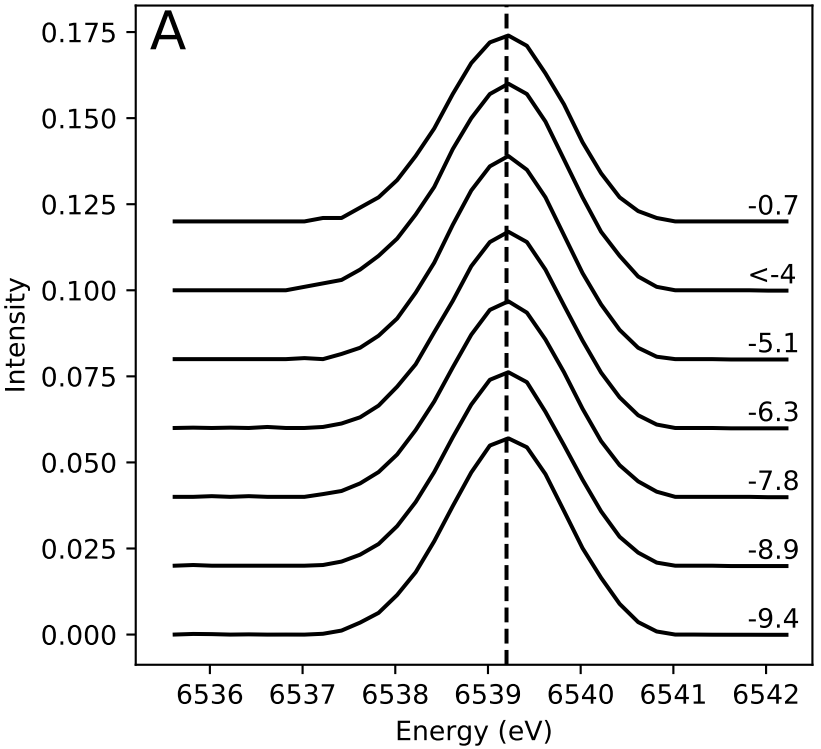
A
Intensity
Energy (eV)
-0.7
<-4
-5.1
-6.3
-7.8
-8.9
-9.4

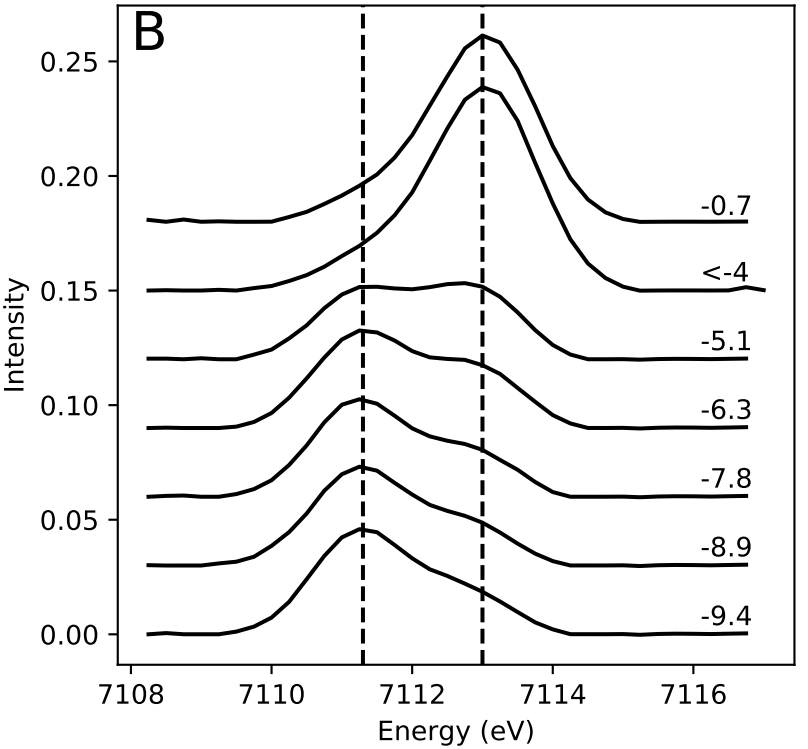
B
Intensity
Energy (eV)
-0.7
<-4
-5.1
-6.3
-7.8
-8.9
-9.4

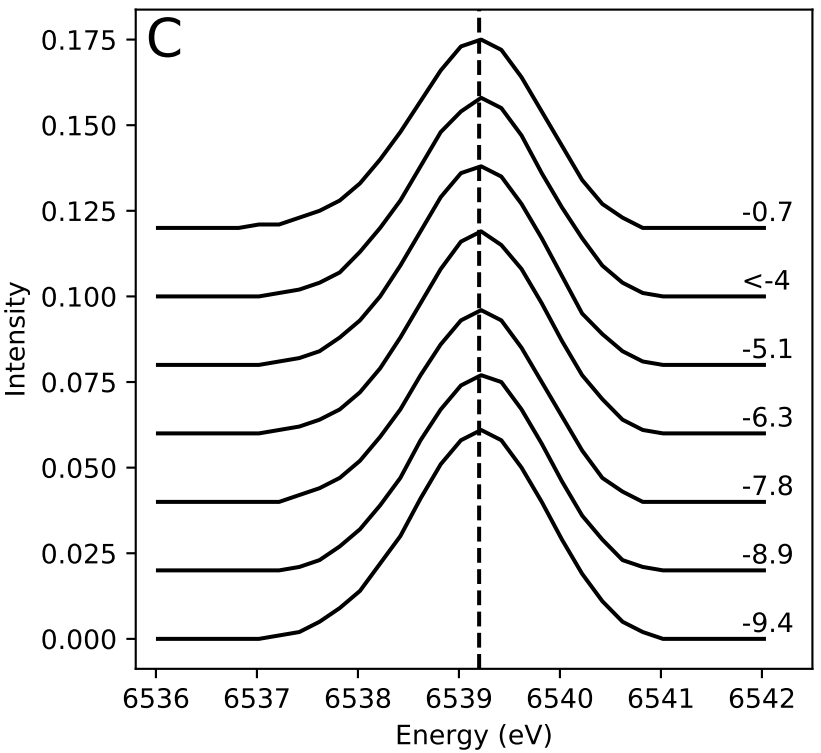
C
Intensity
Energy (eV)
-0.7
<-4
-5.1
-6.3
-7.8
-8.9
-9.4

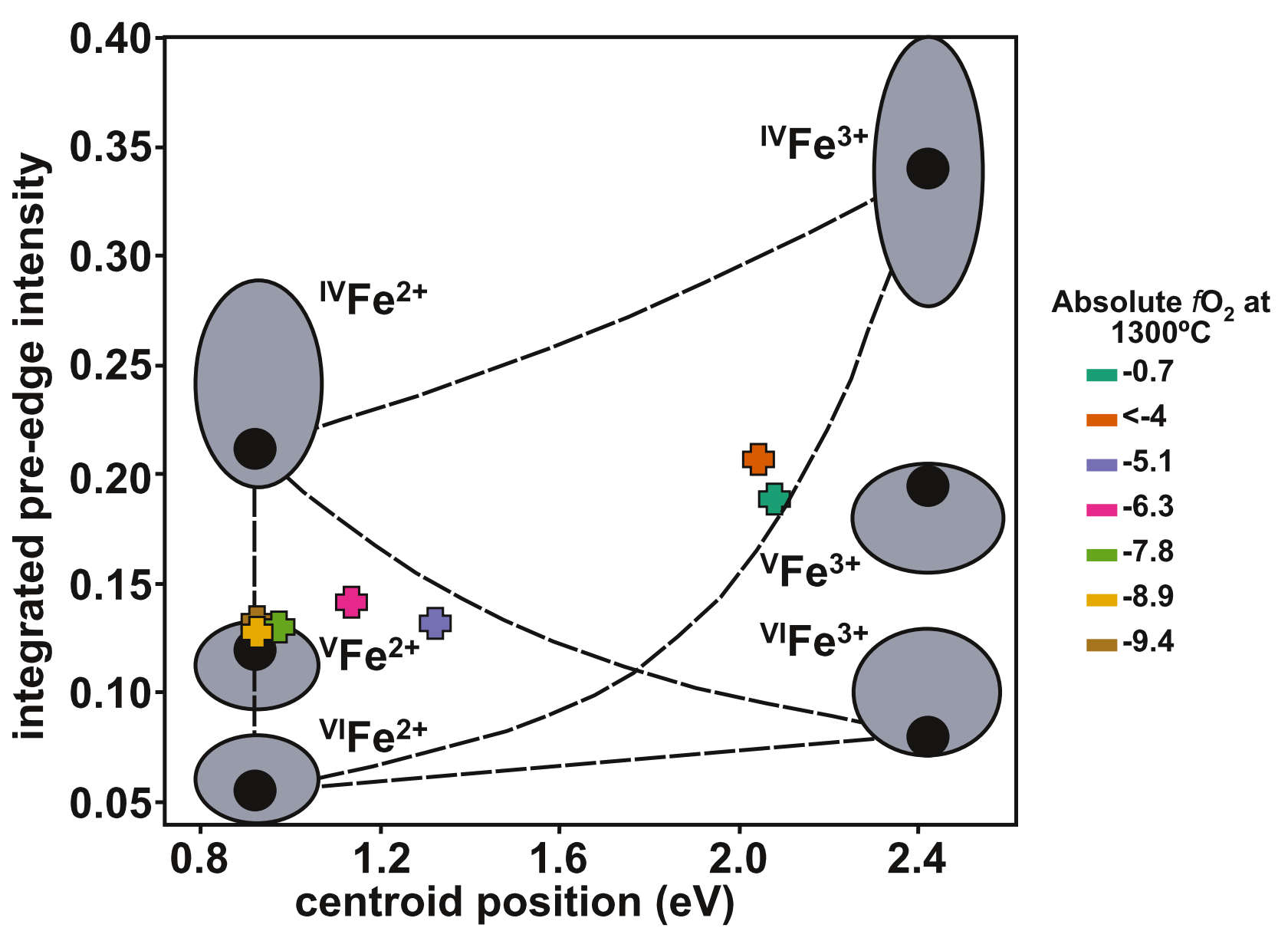
integrated pre-edge intensity
0.40
0.35
0.30
0.25
0.20
0.15
0.10
0.05
0.8
1.2
1.6
2.0
2.4
centroid position (eV)
IVFe3+
IVFe2+
VFe3+
VFe2+
VIFe3+
VIFe2+
Absolute fO2 at 1300ºC
-0.7
<-4
-5.1
-6.3
-7.8
-8.9
-9.4

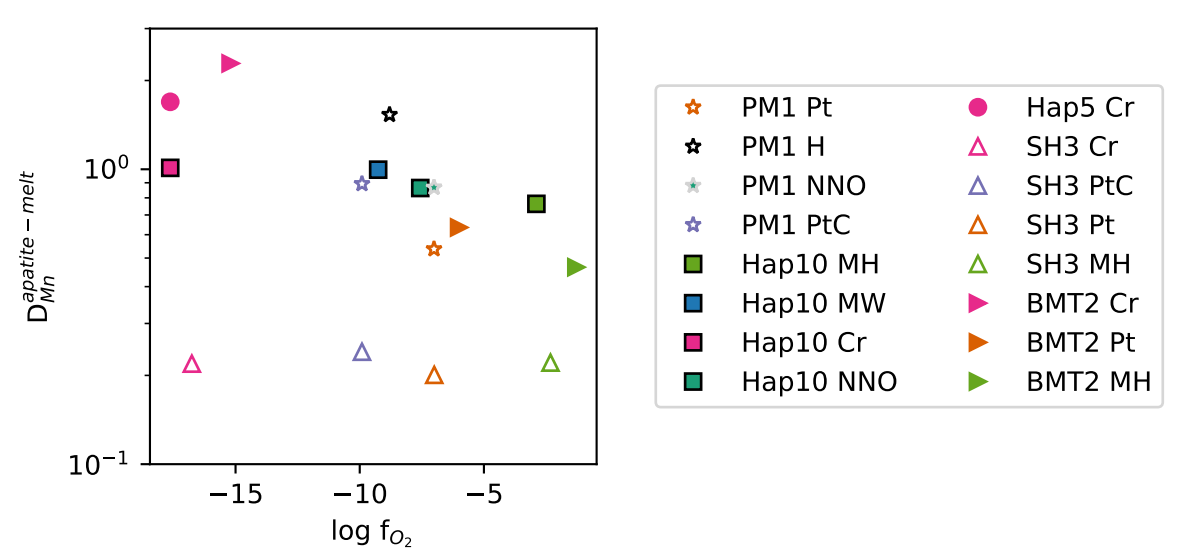
10^0
10^{-1}
$D_{Mn}^{apatite-melt}$
−15
−10
−5
log f_{O_2}
PM1 Pt
PM1 H
PM1 NNO
PM1 PtC
Hap10 MH
Hap10 MW
Hap10 Cr
Hap10 NNO
Hap5 Cr
SH3 Cr
SH3 PtC
SH3 Pt
SH3 MH
BMT2 Cr
BMT2 Pt
BMT2 MH

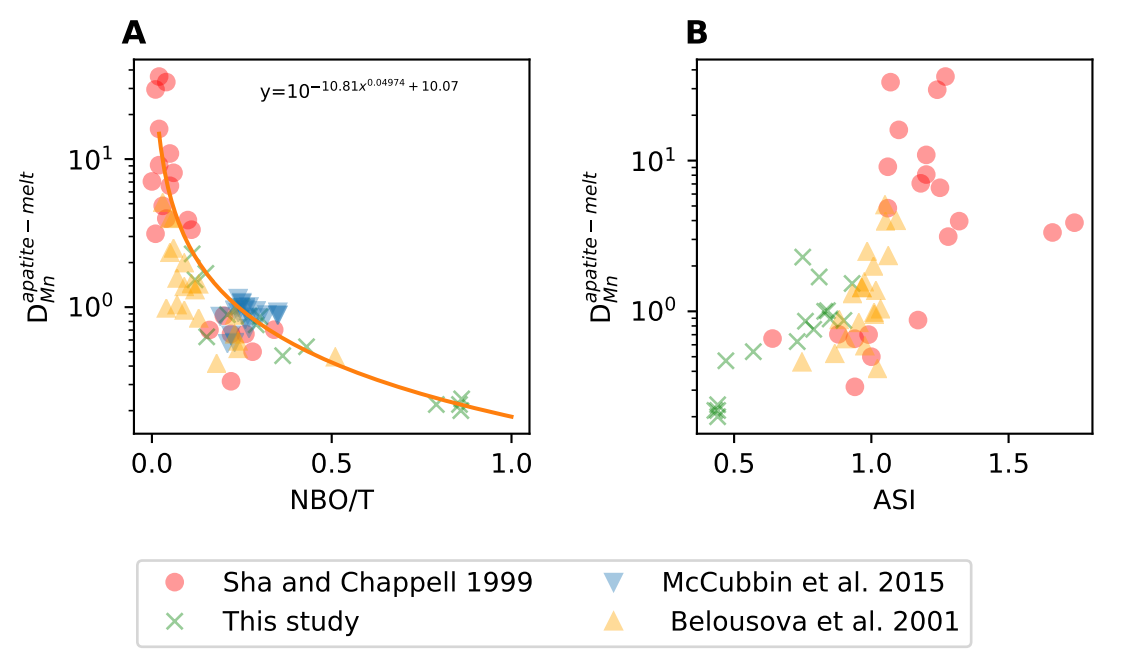
A
B
y=10^−10.81x^0.04974 + 10.07
$D_{Mn}^{apatite-melt}$
10^1
10^0
0.0
0.5
1.0
NBO/T
0.5
1.0
1.5
ASI
Sha and Chappell 1999
This study
McCubbin et al. 2015
Belousova et al. 2001

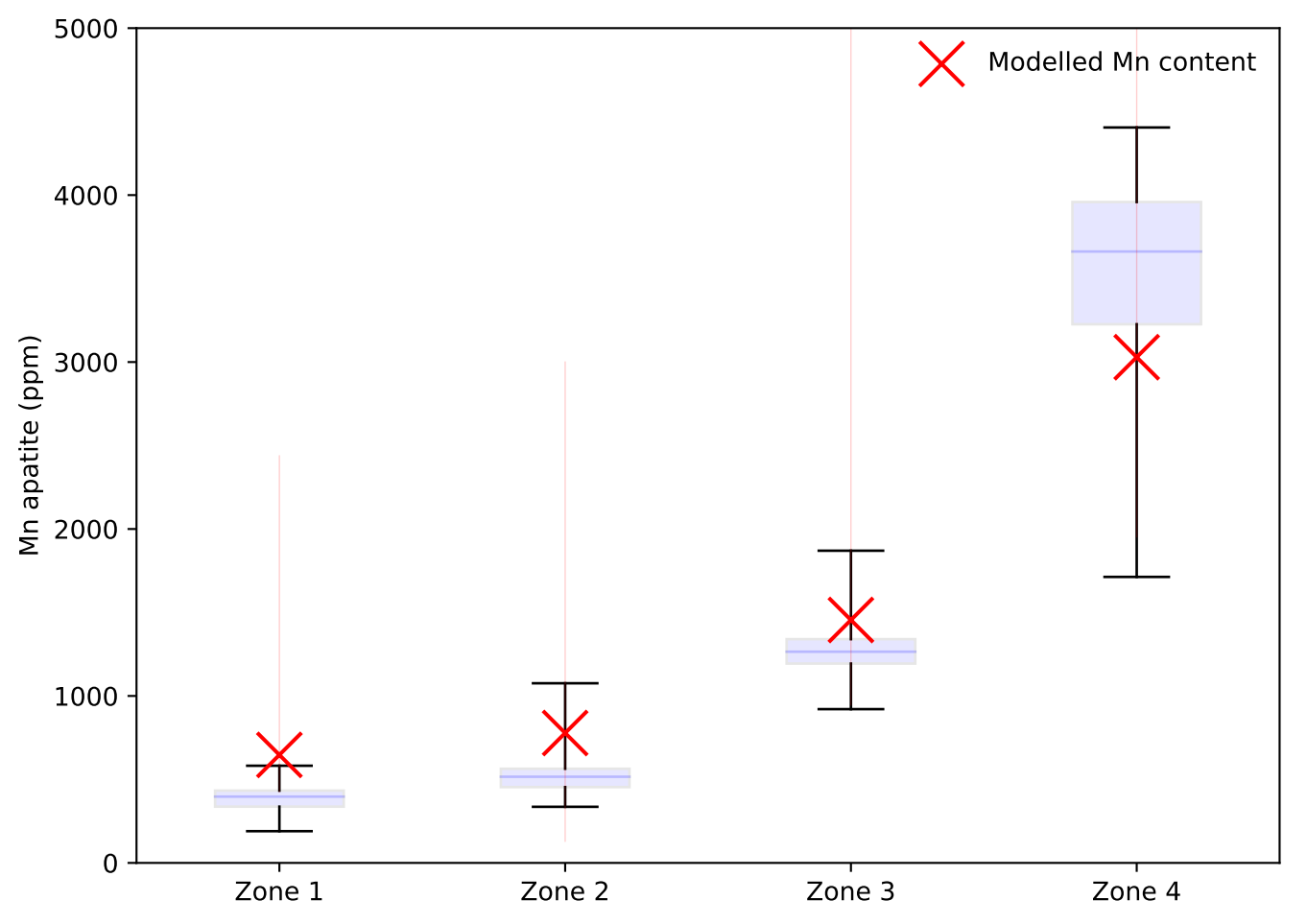
Modelled Mn content
Mn apatite (ppm)
5000
4000
3000
2000
1000
0
Zone 1
Zone 2
Zone 3
Zone 4

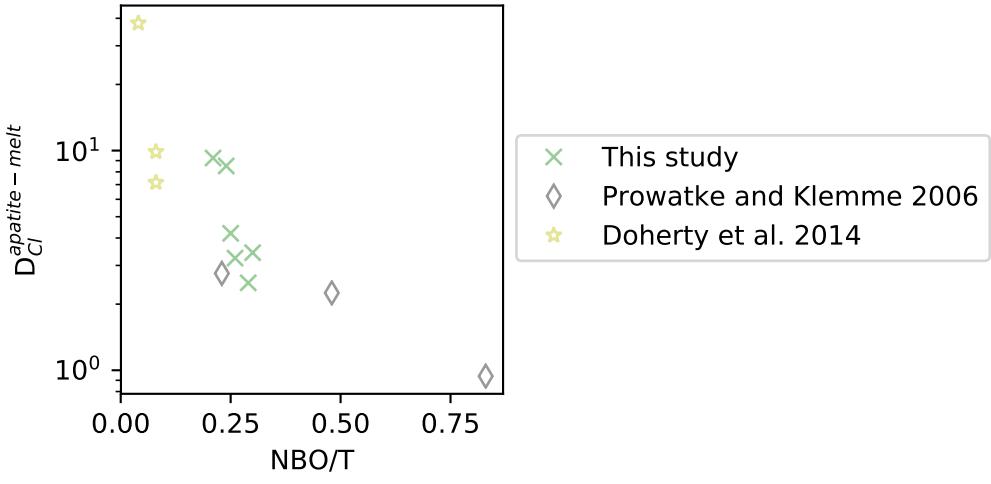
$D_{Cl}^{apatite-melt}$
10^1
10^0
0.00
0.25
0.50
0.75
NBO/T
This study
Prowatke and Klemme 2006
Doherty et al. 2014